ISPRS Journal of Photogrammetry and Remote Sensing 173 (2021) 151–165

Contents lists available at ScienceDirect

ISPRS Journal of Photogrammetry and Remote Sensing

journal homepage: www.elsevier.com/locate/isprsjprs

Automated digital elevation model (DEM) generation from very-high-resolution Planet SkySat triplet stereo and video imagery

Shashank Bhushan [a,*], David Shean [a], Oleg Alexandrov [b], Scott Henderson [c,d]

[a] University of Washington, Civil and Environmental Engineering, Seattle, WA 98195, USA
[b] SGT Inc./NASA Ames Research Center, Intelligent Robotics Group M/S 269-3, Moffet Field, CA 94034, USA
[c] University of Washington, Earth and Space Sciences, Seattle, WA 98195, USA
[d] University of Washington, eScience Institute, Seattle, WA 98195, USA

ARTICLE INFO

Keywords:
Photogrammetry
Stereo
Structure from motion (SfM)
Commercial satellite imagery
SmallSat
CubeSat

ABSTRACT

The Planet SkySat-C SmallSat constellation can acquire very high resolution (0.7 m to 0.9 m) triplet stereo and video imagery with short revisit times, providing an exciting opportunity for global, on-demand 3D mapping of dynamic surface features. However, a lack of suitable processing software, limited geolocation accuracy, and scene-to-scene offsets currently limit the potential for accurate SkySat digital elevation model (DEM) production. We developed an open-source workflow to refine the SkySat-C camera models and improve absolute image geolocation using external reference DEMs, without manual ground control point (GCP) selection. The refined camera models are used to generate accurate and self-consistent DEMs with 2-m posting and orthoimages at native resolution. We present sample DEM products for a triplet stereo collection over Mt. Rainier, USA and two video collections over Mt. St. Helen's, USA. The output DEMs display <1 to 2 m relative and <2 to 3 m absolute vertical accuracy when compared to DEMs generated with stereo image pairs acquired by the DigitalGlobe/Maxar WorldView satellites and airborne LiDAR. Differencing the two SkySat-C video DEMs over Mt. St. Helen's shows elevation change of ~5 to 15 m due to melting of seasonal snow and glacier flow. Our workflow can be scaled for batch processing of SkySat stereo imagery, and extended to other frame camera systems with limited initial geolocation accuracy.

1. Introduction

Digital Elevation Models (DEM) s offer continuous measurements of surface elevation on a regular grid (Deilami and Hashim, 2011). They are widely used in Geographic Information System (GIS) analyses, with applications across multiple disciplines, including Earth science, architecture, reconnaissance and natural hazard monitoring/modeling (e.g., Morrison et al., 2005; Albino et al., 2015; Kim et al., 2015; Brun et al., 2017). In recent decades, the availability of high-quality data from spaceborne optical stereoscopic (e.g., SPOT, ASTER, Cartosat-1, ALOS PRISM) and Synthetic Aperture Radar (SAR; e.g., ERS-1/2, TanDEM-X) instruments has enabled DEM generation and analysis on a global scale. Commercial satellites in sun-synchronous polar orbits (e.g., Maxar/DigitalGlobe WorldView-1/2/3 and GeoEye-1, CNES/Airbus Pleiades) can be tasked to collect very-high-resolution (sub-meter) stereo imagery with resulting DEM vertical accuracy of < 0.2–0.5 m after correction (e.g., d'Angelo and Kuschk, 2012; de Franchis et al., 2014; Noh and Howat, 2015; Shean et al., 2016; Leotta et al., 2019; Zhang et al., 2019). Large archives of accurate, high-resolution DEMs and orthoimages derived from sub-meter commercial imagery have changed the way many geodetic problems are approached, with applications in both regional scale mapping, geodetic change detection studies (e.g., Porter et al., 2018; Howat et al., 2019; Shean et al., 2020; Tian et al., 2012) and detailed temporal analyses of local surface processes (e.g., Willis et al., 2015; Kehrl et al., 2017; Brun et al., 2018; Rounce et al., 2018; Dai et al., 2018).

Growing demand for sub-meter commercial satellite imagery, however, has led to increased competition for limited satellite resources, which can result in missed tasking acquisitions, especially for low-latitude targets with limited time windows (e.g., field campaigns, end of summer melt season on glaciers). Also, most end users have limited or no control of the commercial stereo acquisition geometry, which could be optimized for user-specific applications and target properties. For example, a user might want larger convergence angles for relatively flat

* Corresponding author.
E-mail addresses: sbaglapl@uw.edu (S. Bhushan), dshean@uw.edu (D. Shean), oleg.alexandrov@nasa.gov (O. Alexandrov), scottyh@uw.edu (S. Henderson).

https://doi.org/10.1016/j.isprsjprs.2020.12.012
Received 14 July 2020; Received in revised form 13 November 2020; Accepted 22 December 2020
Available online 22 January 2021

terrain (e.g., Büyüksalih and Jacobsen, 2006), and smaller convergence angles for dense forest canopy and high-relief terrain (e.g., Piermattei et al., 2018; Montesano et al., 2019).

The recent proliferation of low-cost, small imaging satellites ("SmallSats" or "CubeSats") has revolutionized Earth observation, with constellations of inexpensive satellites now offering greater operational capacity and reduced revisit interval (hours-days). Planet (formerly Planet Labs, Inc.) operates multiple constellations of optical imaging satellites, which offer both high resolution (~140 Dove satellites with 3–5 m ground sample distance [GSD]) and very-high-resolution (~19 SkySat-C satellites with 0.7 to 0.9 m GSD) products (Marta, 2019). The Dove constellation provides Planet's flagship PlanetScope archive with "always-on", ~daily global coverage. The SkySat-C constellation operates in tasking mode for mono, triplet stereo or video collection with short repeat interval for small areas.

While these SmallSat constellations can offer improved operational capacity, the instruments and control systems are typically inferior to the larger, more traditional optical imaging satellites. For example, products from Maxar/DigitalGlobe WorldView satellites have absolute geolocation accuracy of < 3–5 m CE90 (DigitalGlobe, 2016), while typical SkySat-C products have geolocation accuracy of < 50 m Root Mean Square Error (RMSE) (Marta, 2019).

1.1. Previous work

Many previous studies document stereo DEM quality for existing commercial sub-meter imaging satellites, but few evaluations are available for SmallSat platforms. d'Angelo et al. (2016) evaluated sample products from the first-generation SkySat-A/B sensors over urban landscapes, offering details on sensor geometry, image acquisition modes, and camera models. They also explored preliminary SkySat sensor geometry/geolocation correction strategies and stereo reconstruction using the SkySat video products. The d'Angelo et al. (2016) geolocation correction study used a National Agriculture Imagery Program (NAIP) reference image basemap to improve geolocation of a SkySat-B mono collect over Chicago, USA. They concluded that the individual SkySat scenes suffered from non-rigid geolocation offsets, which varied across the full SkySat mono collect, requiring multiple ground control points (GCPs) per scene for rectification. After correction, their final orthoimage geolocation accuracy was 5 m RMSE. The d'Angelo et al. (2016) stereo reconstruction study used a subset of scenes from a SkySat-A video collection (60 out of 3600 images) over Las Vegas, USA. To improve input camera models, d'Angelo et al. (2016) automatically tied the video scenes to a reference image basemap using identifiable road networks and ran a bundle adjustment optimization. They then produced 14 individual DEMs via dense correlation of 14 "anchor" images with their respective 20 neighboring images, and created per-pixel mean and median DEM composites. When the median DEM composite was compared to an airborne LiDAR point cloud, the normalized median absolute deviation (NMAD) (e.g., Höhle and Höhle, 2009) of elevation difference values was 1.2 m.

Wan et al. (2016) performed super-resolution experiments on disparity maps obtained by correlating multiple image pairs from a SkySat-A video sequence over an open-pit mine in Usak, Turkey. A sub-pixel registration step was required prior to merging the disparity maps to improve the accuracy of the resolution-enhanced composite disparity maps. Ghuffar (2018) performed experiments for a set of overlapping near-nadir (view angles between 2 to 5°), multi-date, multi-orbit, images from Planet Dove instruments (PlanetScope) over several natural landscapes. They performed a bundle adjustment to reduce the rational polynomial coefficient (RPC) model bias of all input images, generated DEMs from all possible image pairs, and generated a final per-pixel mean DEM composite with elevation difference NMAD values of 4–9 m over "static" surfaces for their test sites (compared to reference DEMs derived from airborne LiDAR and ALOS PRISM stereo images). These previous studies demonstrate that SmallSat/CubeSat imagery can be used for stereo reconstruction and geodetic analysis, but only after the user performs several correction and processing steps, often requiring manual intervention.

1.2. Study objectives

NASA established the Commercial Smallsat Data Acquisition Program in 2017, with a 2019 pilot study to evaluate Planet data for NASA Earth Science research applications. During the course of this pilot study, the program coordinated multiple tasking campaigns with the Planet SkySat-C platforms for a range of priority science targets. The imagery acquired during this pilot is now available to all NASA researchers for further evaluation and analysis (see https://earthdata.nasa.gov/esds/csdap/csdap-pilot-evaluation for further details, (NASA Earth Science Division, 2020)).

To our knowledge, stereo reconstruction using products from the newer SkySat-C instruments has not been documented in the remote sensing literature. Here, we (1) review the SkySat-C instrument specifications, operational modes, and standard products, (2) present a new workflow for SkySat-C sensor geometry correction and image geolocation refinement, (3) describe a workflow for SkySat-C stereo reconstruction and DEM/orthoimage composite generation, (4) evaluate the quality and accuracy of these DEM products, and (5) present two case studies using SkySat-C data to study dynamic glaciers and snow on active stratovolcanoes (Mt. St. Helen's and Mt. Rainier in Washington state, USA). We also present a brief evaluation of popular commercial and open-source Structure from Motion (SfM) software packages for SkySat-C processing.

2. SkySat-C background

2.1. Satellite and instrument description

The SkySat-C constellation consists of 19 small (60 x 60 X 95 cm), lightweight (100 kg) optical imaging satellites, with 13 of the satellites in sun-synchronous orbits (inclinations of ~98.3° and ~95.3° and altitude of ~500 km (Christopherson et al., 2019)). The high inclination angle translates to a equatorial revisit time of 4 to 5 days for any individual satellite (Marta, 2019), but the full constellation includes multiple orbit planes, and can provide sub-daily revisit time nearly anywhere on Earth. Six additional SkySat-C satellites (14 to 19) were launched in August and September 2020 in a mid-inclination orbit (~53°) at lower altitude (~400 km), further improving image ground sample distance (GSD) and revisit times for lower latitudes. All SkySat-C satellites include an active propulsion system which offers improved agility and pointing accuracy over the earlier SkySat-A/B satellites.

The SkySat-C instrument consists of a Ritchey-Chretien Cassegrain f/10.3 optical telescope with 3.6 m focal length and 35 cm primary mirror diameter (Zhai et al., 2018; d'Angelo et al., 2016). The sensor focal plane includes three 5.5 megapixel complementary metal–oxide–semiconductor (CMOS) detectors (2560 by 2160 pixels each) (Marta, 2019) (Fig. 1B). The upper portion of each detector captures panchromatic images, while the lower portion of the detector captures 4-band multispectral images with filters for blue, green, red and near-infrared (NIR) bands. The three detectors are arranged in a "tuning fork" orientation, with detector 2 forward of detectors 1 and 3 (Fig. 1B). Each individual detector has a relatively small ground footprint, with panchromatic image dimensions of ~2.5 km by 1 km (covering ~2.5 km^2) and native Level-1A (L1A) image ground sample distance (GSD) of ~0.9 m at nadir. In June 2020, Planet lowered the orbits of SkySat-C constellation to ~450 km, which should provide a native ~0.7 m GSD at nadir, but these products were not available at the time of our evaluation.

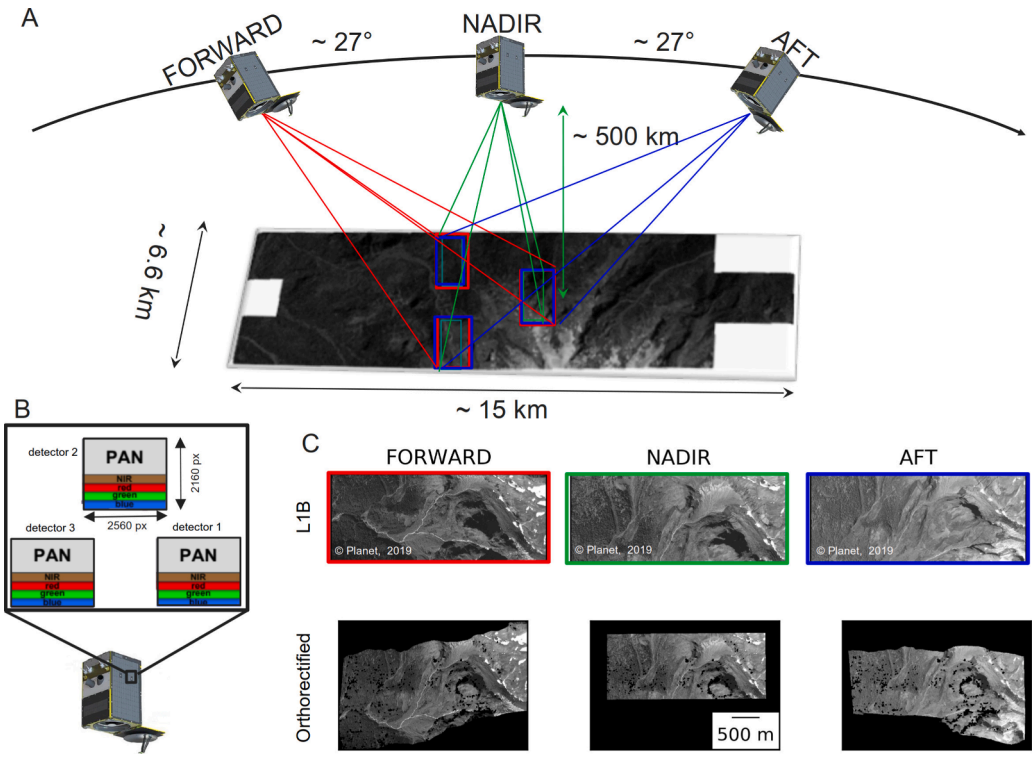

Fig. 1. (A) SkySat-C triplet stereo image acquisition geometry (not to scale). (B) SkySat-C focal plane schematic. (C) Sample Level-1B (L1B) scenes and orthoimages for the same surface features, as viewed by detector 2 with forward, nadir, and aft orientation. Satellite illustration and image data ©Planet, 2019.

2.2. Acquisition modes

The SkySat-C satellite can be operated in multiple acquisition modes, including mono, triplet stereo, and video collection. Products from each acquisition mode are comprised of many overlapping "scenes" acquired by some or all of the three detectors.

2.2.1. Mono collection

The conventional monoscopic products are collected in a "push-frame" mode with all three detectors continuously acquiring image data at a rate of up to 40 frames per second (fps) with exposure cycling to enable high-dynamic range (HDR)-like integration during post-processing. This results in ~900 L1A scenes with ~85–90% along-track overlap between scenes acquired by each detector. The cross-track overlap between scenes from adjacent detectors is ~10%. During post-processing, the scenes undergo a virtual "pushframe" time-delay integration (TDI) and super-resolution enhancement procedure. The resulting Level-1B (L1B) product GSD is ~0.7 m at nadir, with reduced along-track overlap of ~15% between adjacent scenes from the same detector. The typical combined mono collect ground footprint dimensions are ~6.6 x 15 km, covering ~90 km^2 (Fig. 1A).

2.2.2. Triplet stereo collection

The triplet stereo acquisition mode includes three overlapping mono collections on the same pass, with forward-facing (27° off-nadir), nadir, and aft-facing (-27° off-nadir) geometry (Fig. 1). The collections are separated by ~35 s.

2.2.3. Video collection

The SkySat-C satellites can also collect 30 fps high-definition (HD) video for a fixed ground target over a period of 30, 60, 90 or 120 s. Only the panchromatic portion of detector 2 (Fig. 1B) is used during video collection, with no exposure cycling, providing ~0.9 m GSD at nadir (Fig. 2). The resulting video includes ~900–3600 overlapping scenes acquired for a range of off-nadir angles spanning approximately −45° to +45° for a symmetrical ~120-s video (Fig. 2A), resulting in an average angular separation of ~0.022° between consecutive scenes.

2.3. Camera models

Planet provides rational polynomial coefficient (RPC) camera models for all L1A and L1B SkySat scenes. These RPC models are generated using keypoint matches between the individual L1A images and a proprietary reference orthoimage basemap (derived from National Agriculture Imagery Program [NAIP], Advanced Land Observation Satellite [ALOS], Landsat-8, and other image sources), with corresponding elevation data extracted from regional and global DEMs (e.g., National Elevation Dataset [NED], Shuttle Radar Topographic Mission [SRTM], InterMap World 30) (Marta, 2019). This RPC generation method works well for most cases, but can be problematic over dynamic surface features like glaciers and landslides, which display time-variable vertical and horizontal surface displacements. In addition, images acquired over non-planar terrain with variable relief can have additional geolocation issues due to geolocation errors in the original basemap and inconsistencies between the DEM used for SkySat RPC elevation control and that used for orthorectification of the basemap imagery. In such cases, the RPCs for overlapping SkySat scenes can suffer from offsets which are non-rigid in nature. In addition to the RPC camera models, the video products include a rigorous, custom pinhole camera model and relevant metadata (i.e., ephemeris, attitude) for each scene.

3. Methods

3.1. Overview

We developed automated processing workflows for SkySat products acquired using the triplet stereo and video acquisition modes (Fig. 3), which can also be extended to process overlapping mono image collections with suitable geometry. The workflows exclusively use open-source tools, including the Ames Stereo Pipeline (ASP, version 2.7.0

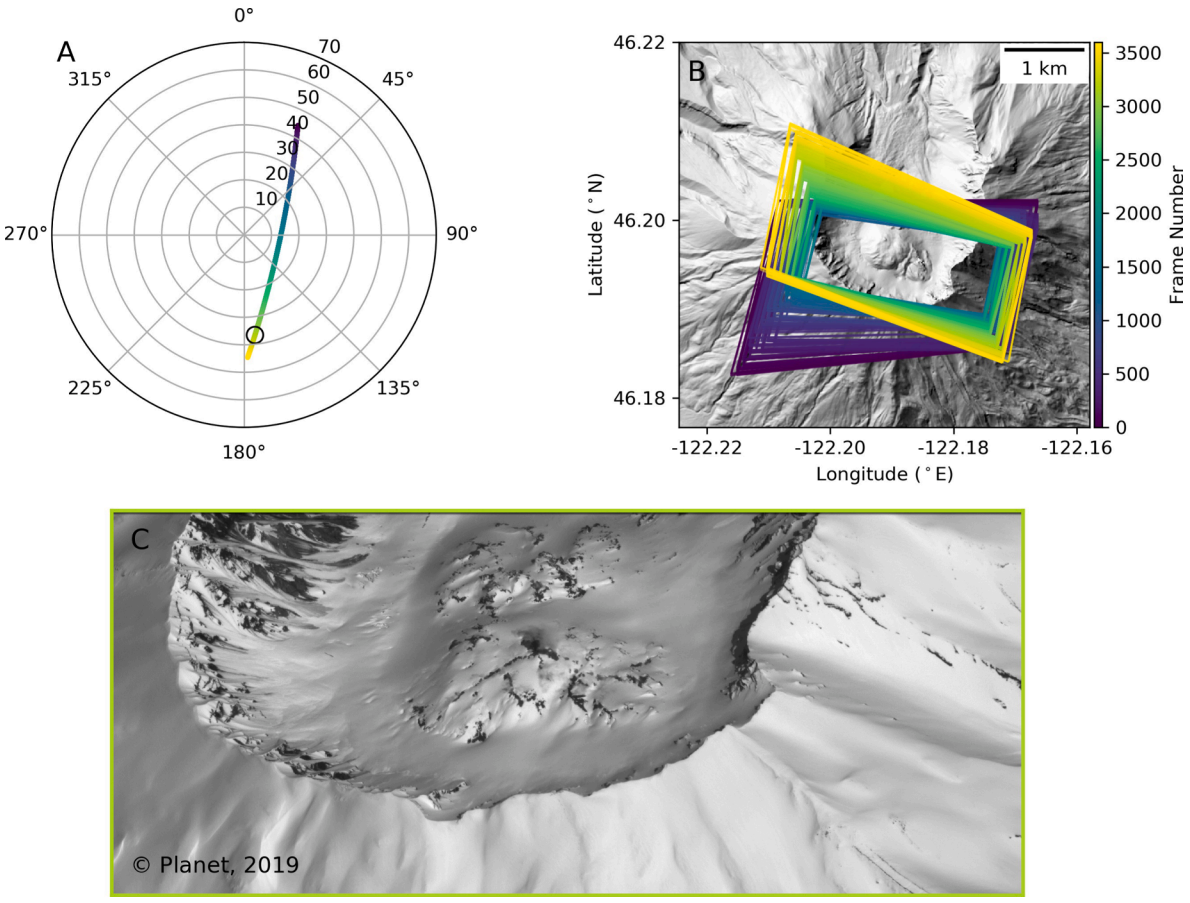

Fig. 2. SkySat-C 120-s video test case for Mt. St. Helen's, WA, acquired April 20, 2019. (A) Skyplot showing SkySat-C video acquisition geometry (satellite azimuth and elevation angles) relative to ground target center (−122.192°E, 46.195°N). (B) Footprints for all video scenes plotted over shaded relief map from reference WorldView DEM composite. (C) Sample off-nadir video scene (frame #3143), corresponding to black circle in (A). L1A Image data in (C) is ©Planet, 2019.

(Beyer et al., 2018, 2020; Shean et al., 2016)) and custom Python tools to perform camera model refinement, stereo reconstruction and co-registration to reference elevation data without manually identified GCPs. The **`skysat_stereo`** (Bhushan et al., 2020) code repository accompanying this manuscript contains processing libraries, wrapper scripts and additional documentation of these workflows. The main steps in the common SkySat processing workflow include (1) overlapping stereo scene identification, (2) bundle adjustment, (3) pairwise stereo reconstruction, (4) DEM compositing, (5) DEM co-registration and (6) orthomosaic generation (Fig. 3). The following sections offer details on each processing step, and we reference the corresponding software utility names in bold (e.g., **`stereo_corr`**).

3.2. Stereo pair identification

The first step in our workflow is the selection of overlapping scene pairs to be used for feature matching and camera refinement during bundle adjustment and the successive pairwise stereo reconstruction procedure. The strategy for this step depends on the input product type, as described in the following sections.

3.2.1. Triplet stereo

For the L1B triplet stereo products, we compute a list of all overlapping scene pairs using the original RPC models (**`skysat_overlap.py`**). A typical SkySat triplet stereo collection will produce ~800 unique scene pairs.

3.2.2. Pairwise video stereo

Pair identification for the SkySat video scenes is more flexible, as all scenes inherently overlap, with negligible perspective difference between any two consecutive video scenes (average convergence angle of ~0.022°). Pairs must be selected to appropriately balance performance (eliminating redundant processing), vertical accuracy of triangulated points, and feature matching success for the target terrain characteristics. In general, a larger pair convergence angle will improve triangulated position accuracy (e.g., Delon and Rougé, 2007), but the increased perspective difference can lead to difficulties during feature matching.

Our video pair selection workflow first selects a subset of "reference" scenes from the full 30 fps video sequence using either a user-specified total number (n) of scenes spaced equally across the full video sequence, or a fixed sampling interval (e.g., every m^{th} scene) (Fig. S1A) (**`skysat_preprocess.py`**). We prefer the strategy of sampling user-specified total number of scenes, as the first and last scenes are always included. After a subset of scenes is identified, stereo pairs are identified by pairing each reference scene with several neighbouring ("source") scenes from the same subset using a user-defined interval p (Fig. S1B). By design, a larger interval (p) between the reference and source scenes translates to a higher convergence angle for the resulting stereo pairs. This strategy offers a good compromise between performance and optimum stereo geometry, but can exclude scenes near the beginning and end of the video sequence, resulting in a smaller ground footprint of the final DEM composite. To avoid this limitation, our workflow includes additional pairs with smaller convergence angles at the beginning and end of the video sequence (Fig. S1B).

For this study, we extracted a subset of $n = 60$ equally spaced scenes from 120-s SkySat video samples (Fig. S1A), resulting in consecutive scenes with an average angular separation of ~1.36°. Feature matching during subsequent bundle adjustment (Section 3.4) was limited to 20

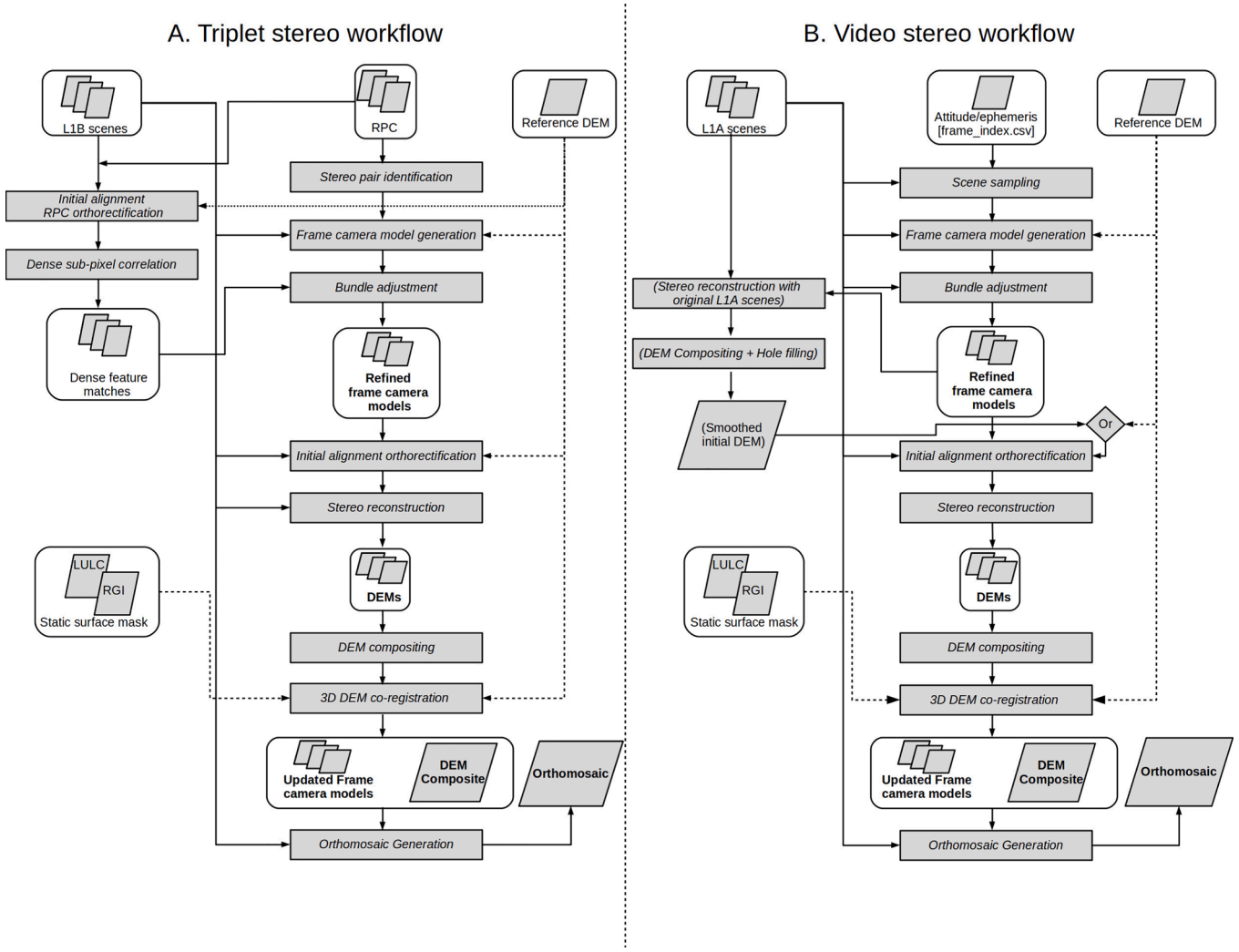

Fig. 3. Flowchart outlining workflow for (A) SkySat-C triplet stereo and (B) video stereo products. Processing steps are denoted by gray rectangles, with products denoted by gray parallelograms. External inputs (e.g., reference DEMs) are connected by dashed lines while optional processing steps and products are enclosed in parentheses. Final output products are identified with bold text.

consecutive scenes from this 60-scene subset, with maximum average convergence angle of ~27°. For stereo reconstruction, pairs were created from the 60-image subset using an interval of $p = 10$ between the reference and source scenes. Corresponding convergence angles were between 11° to 18°, with additional pairs formed near the beginning and end of the video sequence (Fig. S1B), resulting in a total of 62 stereo pairs.

3.2.3. Multi-view video stereo

We implemented and tested an experimental multi-view stereo (MVS) workflow which simultaneously processes many scenes, rather than multiple independent pairs. We follow the approach described by d'Angelo et al. (2016), processing k user-selected reference scenes with their respective o neighboring scenes from the subset of n video scenes (Fig. S1C). For this study, we used $k = 14$ and $o = 20$, which produced 14 multi-view DEMs from the subset of $n = 60$ scenes, in contrast to the 62 DEMs produced by the pairwise video stereo workflow (Section 3.2.2).

3.3. Frame camera model generation

After identifying a subset of overlapping scenes, we use the ASP `cam_gen` utility to produce frame camera models for each scene. We use a simple pinhole model, as the relatively long focal length and small detector size of the SkySat-C instrument does not require a more complex lens distortion model. We assume a focal length of 3.6 m and pixel pitch of 6.5 and 5.2 μm for the L1A and L1B scenes, respectively.

The **`cam_gen`** tool performs camera resection (e.g., Mikhail et al., 2001) using the above camera intrinsics (interior orientation) and a known ground footprint to solve for the corresponding camera extrinsics (exterior orientation: position and orientation) with least-squares minimization. The footprint can be estimated using the original L1B RPC camera model and an external reference DEM. When available, we directly use available footprint corner coordinates extracted from the frame_index.csv metadata distributed with L1A video products, with height values sampled from a reference DEM. The L1A metadata also includes Earth-centered, Earth-fixed (ECEF) camera positions that are used as an initial estimate for camera position during resection.

3.4. Bundle adjustment and camera model refinement

Inaccurate camera extrinsics can introduce systematic horizontal and vertical error in DEMs from individual stereo pairs (e.g., Mikhail et al., 2001) and overlapping DEMs from multiple pairs (Ozcanli et al., 2016; Marí et al., 2019). To mitigate these issues, our workflow (**`ba_skysat.py`**) uses known camera intrinsics and a bundle adjustment technique (e.g., Triggs et al., 2000) to iteratively refine camera extrinsics (position and orientation) by minimizing reprojection errors for triangulated points from all input scenes (e.g., Amer, 2006).

Prior to the optimization, keypoint matches are automatically computed between overlapping scenes to define the optimization constraints and establish connections between the individual frame camera models. During initial optimization, we prioritize self-consistency between the full set of camera models, which can introduce some arbitrary drift of the triangulated match points and the entire camera set in space. To mitigate this issue during the triplet stereo processing, our workflow fixes the absolute position and orientation of the first three scenes captured by detector 1 in both the forward and nadir views (i.e., the first three stereo pairs involving detector 1), allowing all other camera models to float during initial optimization. A second round of bundle adjustment is then performed with all camera models fixed except those comprising the first three stereo pairs. For the video products, we allow the entire camera set and triangulated match points to float during initial bundle adjustment optimization, and then shift the entire self-consistent camera set back to its original location (defined by initial ground footprints in original L1A metadata) using a single transformation with translation and rotation components.

The above strategy requires a relatively uniform distribution of keypoint matches between overlapping scenes. This criterion is easily fulfilled by the video collections due to significant overlap between scenes and the smaller convergence angles. However, keypoint matching between overlapping scenes in the triplet stereo collections can fail due to the large perspective differences (convergence angles of ~27° and ~55°), especially over challenging terrain like mountains and forests. As a result, several overlapping scene pairs can have a sparse and/or non-uniform spatial distribution of keypoint matches, which can adversely affect the joint refinement of all camera models for the triplet stereo collection.

To avoid this issue, we use a dense, uniform grid of keypoint matches for each overlapping stereo scene pair (e.g., Dehecq et al., 2020). In this method, the L1B images are orthorectified using the original camera models and a reference DEM. Disparity maps are produced between the orthorectified images using ASP's dense sub-pixel correlation routines, and keypoint matches on a regular grid are extracted from these dense disparity maps. These matches are then back-projected into the original sensor coordinate system with the same camera model and DEM used during orthorectification (Fig. S2), and the resulting keypoint matches from each pair are used during bundle adjustment of all L1B scenes. The dense keypoint matches on a systematic grid can offer improved results over the sparse keypoint matches obtained by SIFT/SURF operators (Fig. S2). This strategy also helps to prevent large shifts in the position and orientation of cameras with fewer overlapping scenes, such as those on the periphery of the triplet stereo collection camera set.

3.5. Stereo reconstruction

After refining extrinsics for all cameras, we use the ASP `stereo` utility for pairwise stereo correlation and triangulation. Our stereo processing routine (**`skysat_stereo_cli.py`**) is similar to the workflow described in Shean et al. (2016), except for the stereo correlation steps (disparity initialization and refinement), where we prefer ASP's implementation of the More Global Matching algorithm (MGM) (Facciolo et al., 2015) and Bayes Expectation–Maximization (EM) affine-adaptive sup-pixel refinement (Nefian et al., 2009). The combination of MGM matching algorithm and the Bayes EM affine-adaptive sup-pixel refinement offers more detail in the output DEMs, while also reducing blunders and artifacts for scenes with repetitive texture and sites with steep relief.

As described in Shean et al. (2016), the initial alignment orthorectification of input scenes prior to stereo reconstruction removes most terrain-induced disparity, which improves image alignment, correlator performance and dense disparity map quality. This orthorectification can be performed using either a pre-existing reference DEM (e.g., SRTM) or a gap-filled, "smoothed initial DEM" derived from an earlier `stereo` run using ASP's default block-matching correlator with the original or downsampled L1A/L1B scenes (e.g., Dehecq et al., 2020; Deschamps-Berger et al., 2020).

After initial alignment orthorectification, we use MGM and sub-pixel refinement to produce dense disparity maps for each stereo pair, followed by the default ASP disparity map filtering. Our workflow uses default MGM correlation and refinement kernel sizes of 7 x 7 pixels and 15 x 15 pixels, respectively. For input scenes with limited texture (e.g., fresh snow), we recommend using larger correlation and refinement kernels of 9 x 9 and 21 x 21 pixels, respectively.

For the pairwise stereo processing workflow, we generate a dense point cloud for each stereo pair using the filtered disparity map, refined camera models and the standard ASP stereo triangulation routine (**`stereo_tri`**). For the SkySat video multi-view stereo workflow (Section 3.2.3), we perform a joint triangulation that combines all disparity maps computed between a reference scene and each of the 20 neighbouring scenes (Slabaugh et al., 2001).

Regardless of pairwise or MVS triangulation strategy, our workflow generates gridded DEMs from the output dense point clouds using the ASP **`point2dem`** utility. We use a DEM posting (output grid cell size) of 2 m and universal transverse mercator (UTM) projection, with the appropriate UTM zone determined by the center latitude and longitude of the point cloud.

3.6. DEM compositing

Our workflow uses the ASP **`dem_mosaic`** tool to produce per-pixel weighted-average and median DEM composites from all DEMs generated during pairwise stereo reconstruction (**`skysat_dem_mos.py`**). We also compute additional per-pixel metrics, such as the count and NMAD of valid elevation values, which are used to evaluate the relative accuracy of the output DEM composites. These metrics are used to filter the video DEM composites, removing any values with per-pixel DEM count of less than 2 and per-pixel elevation NMAD of greater than 5 m.

3.7. DEM co-registration: absolute geolocation refinement

The bundle adjustment step (Section 3.4) improves the self-consistency of the full set of SkySat camera models. If successful, the resulting pairwise DEMs should also be self-consistent, with limited relative horizontal and vertical offsets. However, without incorporating accurate GCPs during bundle adjustment, the absolute geolocation accuracy of the DEMs will be limited by the absolute geolocation accuracy of the initial L1A/L1B camera models provided by Planet (<50 m for SkySat products (Marta, 2019)).

To improve SkySat DEM geolocation accuracy, our workflow uses the ASP `pc_align` utility to align the per-pixel median DEM composite with an external reference DEM that has relatively high resolution and accuracy. This tool ingests the raster DEMs as regularly spaced point clouds with a point at each grid cell center. Horizontal point coordinates are computed from the raster geotransform, and vertical point coordinates are obtained from the raster cell values. A sample containing 75% of the points over "static" surfaces (e.g., exposed bedrock) is extracted from each point cloud, and the point-to-plane Iterative Closest Point (ICP) algorithm (Pomerleau et al., 2013) is used to determine the rigid-body transformation (3-D rotation and translation) needed to co-register these samples.

The full point cloud is then transformed and regridded to produce a new DEM with improved geolocation. The final absolute vertical accuracy of the DEM is estimated using the median and NMAD of the residual elevation difference values between the co-registered SkySat DEM and the reference DEM over static surfaces (e.g., Shean et al., 2016).

The same transformation is used to update the set of self-consistent frame camera models (e.g., Dehecq et al., 2020; d'Angelo and Reinartz, 2012) which are needed for subsequent orthorectification steps. Refined RPC camera models can also be generated from these transformed frame camera models.

3.8. Orthomosaic generation

We use the ASP **mapproject** utility to create final orthoimages at native GSD for all input L1A/L1B SkySat scenes using the refined frame camera models and co-registered DEM composite. We then generate several orthoimage composite and mosaic products using the ASP **dem_mosaic** utility. These include a per-pixel weighted-average composite, a per-pixel median composite, and a blended mosaic product that prioritizes input orthoimages with higher resolution.

4. Case studies

We now present two case studies to demonstrate the capabilities of our SkySat stereo processing workflows, evaluate the accuracy of final products, and demonstrate potential for quantitative Earth science research applications. The supplementary materials also include products and results from two additional SkySat triplet stereo datasets (Fig. S3) and five additional SkySat video datasets (Fig. S4) acquired, processed and evaluated during the NASA CSDAP Pilot study.

4.1. SkySat triplet stereo

Our first case study involves an August 27, 2019 triplet stereo collection over the western flank of Mt. Rainier in Washington state, USA (Fig. 4). This site covers a diverse landscape including glaciers, exposed bedrock, river valleys, and dense conifer forests, with over 2 km of total relief.

4.1.1. Reference DEM

We produced Digital Surface Models (DSMs) at 1 m and 10 m posting from publicly available airborne LiDAR data (hereafter referred to as "LiDAR reference DEM") collected over Mt. Rainier during 2007 and 2008 (Robinson et al., 2010). See **lidar_processing** in Bhushan et al. (2020) for additional details. The LiDAR point cloud has RMSE of 0.037 m with a 2-sigma spread of 0.072 m when compared to GPS check points over flat roads (Robinson et al., 2010).

The 10-m LiDAR reference DEM was used to initialize the SkySat frame camera models and perform initial alignment orthorectification of input scenes before stereo reconstruction. We assume that both the SkySat DEMs and LiDAR DEM capture the same canopy surface. Exposed static surfaces needed for co-registration and accuracy assessment (Section 3.7) were identified in the 1 m LiDAR reference DEM by

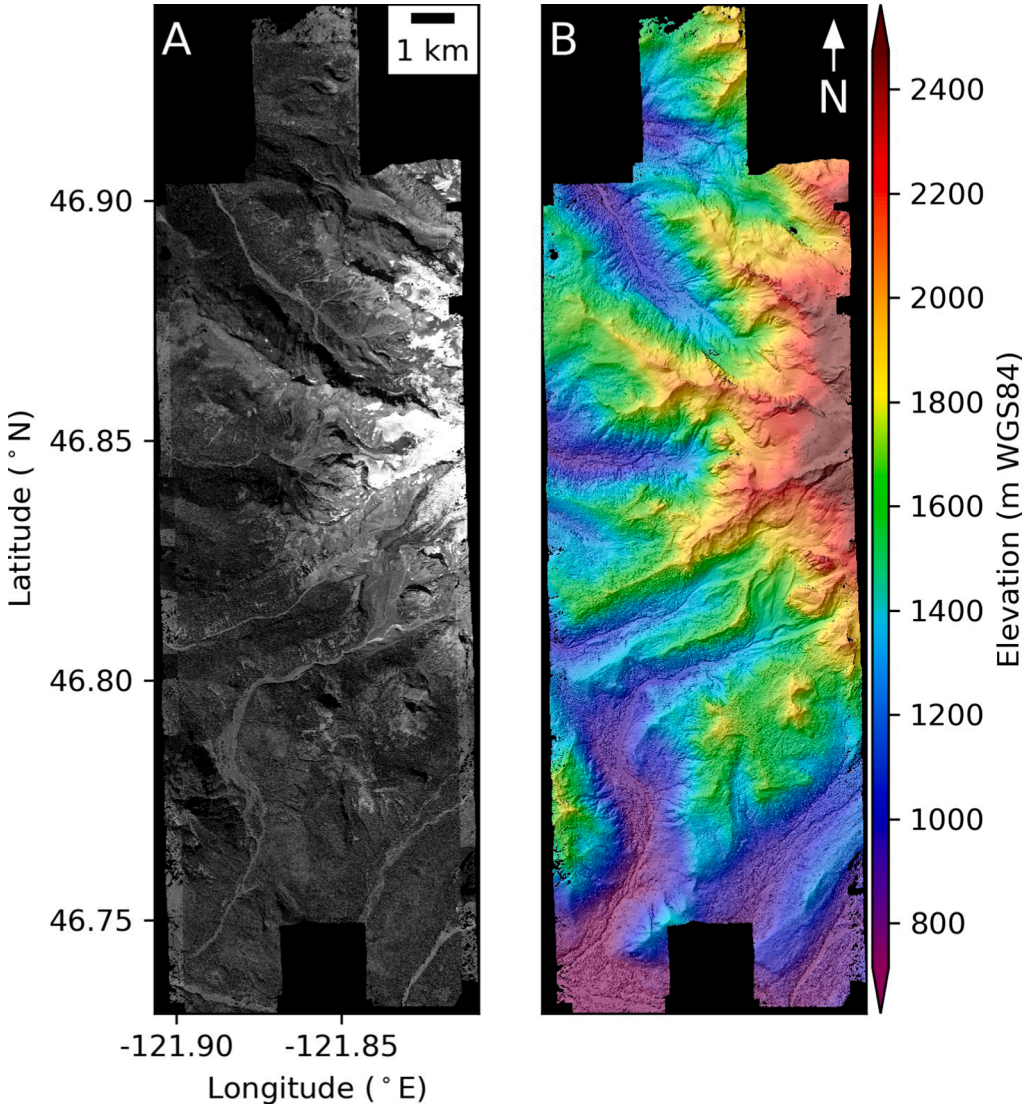

Fig. 4. SkySat triplet stereo products, acquired August 27, 2019 (identifiers: 20190827_214711_ssc9, 20190827_214745_ssc9, 20190827_214821_ssc9) (A) Orthomosaic with sort order based on orthoimage resolution, and (B) median DEM composite. These final products were derived from L1B imagery that is ©Planet, 2019.

masking forested areas (as defined by the 2016 National Land Cover Database (Dewitz, 2019)) and glacier/snowfield polygons defined by the Randolph Glacier Inventory v6.0 (RGI Consortium, 2017). See the **`dem_mask.py`** utility in the **`dem_coreg`** package (Shean et al., 2019) for additional details.

In order to evaluate the influence of reference DEM quality on the final accuracy of the output SkySat DEM composite, we also prepared a reference DEM using the void-filled, 1-arcsecond (~30 m posting) SRTM-GL1 ellipsoidal DEM (Farr et al., 2007; NASA Shuttle Radar Topography Mission (SRTM), 2013), which is hereafter referred to as the "SRTM reference DEM".

4.1.2. Data processing

We ran the full SkySat triplet stereo workflow described in Section 3 using each of the two reference DEMs. We also reran the workflow without the camera model refinement and bundle adjustment steps, using the original L1B RPC camera models provided by Planet.

We evaluated the relative accuracy of the output SkySat DEM products over different landcover ("forest", "non-forest", see Section 4.1.1) and terrain (slope $<=$ 10°, slope $>$ 10°) classes. To avoid including true elevation change since the reference DEM acquisition date (2000 and 2007/2008), we estimated the absolute accuracy of the 2019 SkySat DEM products over "non-glacierized" surfaces (including forest classes), and "exposed static surfaces" ("non-glacierized, non-forest" classes).

4.1.3. Results

The SkySat triplet stereo workflow using refined camera models provided a considerable improvement in the relative accuracy of the DEM composite (Fig. 5D) compared to the workflow using the original L1B RPC camera models (Fig. 5B). We observe improvements in scene-to-scene alignment (reduced feature offsets at seam boundaries) in the corrected orthomosaic and DEM composite. The median of the per-pixel NMAD values for the full DEM composite ("Full area" in Fig. 6A) was reduced from 3.59 m when using the original L1B RPC models (Fig. 5B) to only 0.73 m when using the refined frame camera models (Fig. 5D). Much of the residual per-pixel spread can be attributed to variable landcover type (e.g., vegetation) and terrain characteristics (e.g., steep relief), with reduced per-pixel NMAD values observed over "non-forest" pixels and surface slopes $<=$ 10° (Fig. 6A).

Our camera refinement workflow also improved the absolute accuracy of the SkySat triplet stereo DEM composite as compared to the 1-m LiDAR reference DEM (Fig. 5E). The absolute vertical elevation difference over static surfaces is ~ ±2 m near the center of the triplet stereo collect footprint, with higher offsets (up to ~ ±10 m) near the margins, which primarily cover forested areas (Fig. 4). We observe negligible residual bias (0.12 m) and limited spread (2.49 m NMAD) over "exposed static surfaces" (Fig. 6B). We also observe real elevation change signals over glaciers between the ~2007/08 LiDAR reference and the 2019 SkySat DEMs (Fig. 5E), with thinning near glacier termini and thickening upstream, as has been documented by other recent studies (Sisson et al., 2011; Menounos et al., 2019).

We obtain comparable relative accuracy for the SkySat DEM composites produced using the LiDAR and SRTM reference DEMs (Fig. S5). The observed median (±NMAD) elevation difference between the two SkySat DEMs is 1.35 (±2.08) m (Fig. S5B), and this can be partly attributed to offsets between the two reference DEMs (Fig. S5A). After relative co-registration of the two SkySat DEMs, the elevation difference values are reduced to 0.12 (±1.63) m (Fig. S5C). The residual elevation differences in Fig. S5C are likely related to artifacts over vegetation and steep slopes introduced during the initial alignment orthorectification step using the SRTM reference DEM, potentially related to the reduced accuracy and variable penetration (Fig. S5A) of the C-band radar (e.g., Kellndorfer et al., 2004).

The reference DEM analysis confirms that high-quality SkySat DEMs can be produced using publicly available coarse-resolution reference DEMs like SRTM. This finding is relevant for most locations across the globe that do not yet have LiDAR or stereo-derived reference DEMs.

4.2. SkySat video stereo

Our second case study involves multiple SkySat video collections over Mt. St. Helen's in Washington state, USA (Fig. 7). Geologically, Mt. St. Helen's is an extremely dynamic system with large elevation change signals on short timescales due to active volcanism (e.g., Kennedy and Russell, 2012), dynamic glaciers (e.g., Schilling et al., 2004), mass wasting, seasonal snow accumulation, and wind/avalanche snow redistribution. The steep walls of the summit crater and volcanic domes provide an opportunity to evaluate the SkySat video multi-view stereo products over terrain which is notoriously challenging for traditional

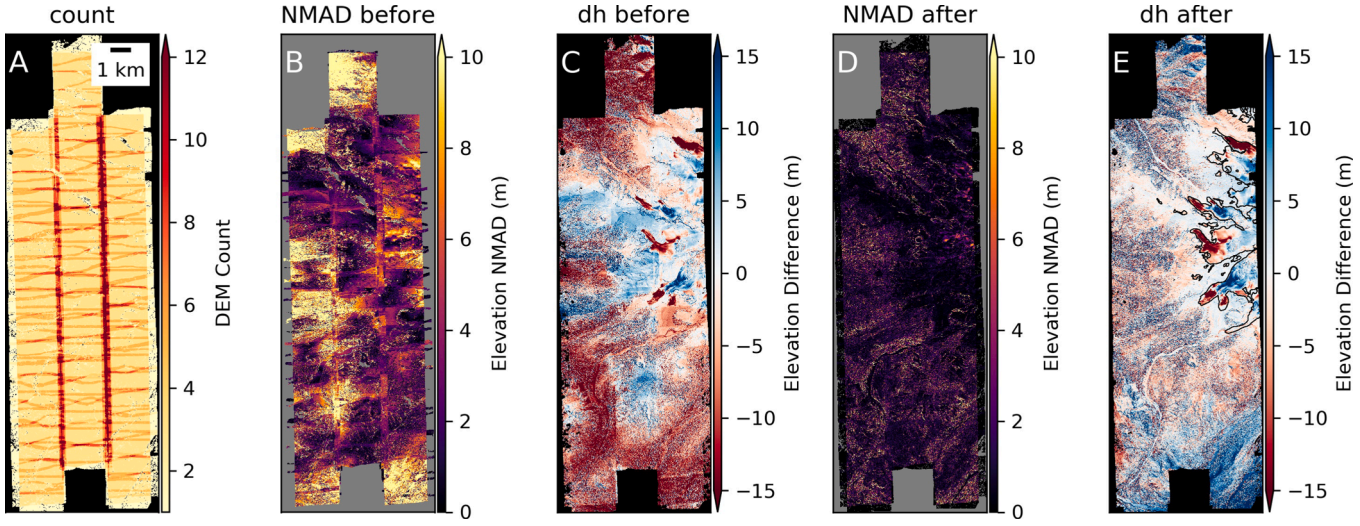

Fig. 5. Mt. Rainier SkySat triplet stereo case study metrics. (A) DEM Count Map. Per-pixel NMAD and elevation difference between SkySat DEM composite and 1 m LiDAR reference DEM (B,C) without ("before") and (D,E) with ("after") bundle adjustment and camera model refinement. Our workflow with refined camera models improved both relative (D) and absolute (E) accuracy. Black lines in (E) show glacier and perennial snowfield outlines from the Randolph Glacier Inventory (RGI) v6.0 (RGI Consortium, 2017). Glacier thinning, especially at lower elevations, is apparent between the ~2007/08 timestamp of the LiDAR reference DEM and the 2019 SkySat DEM.

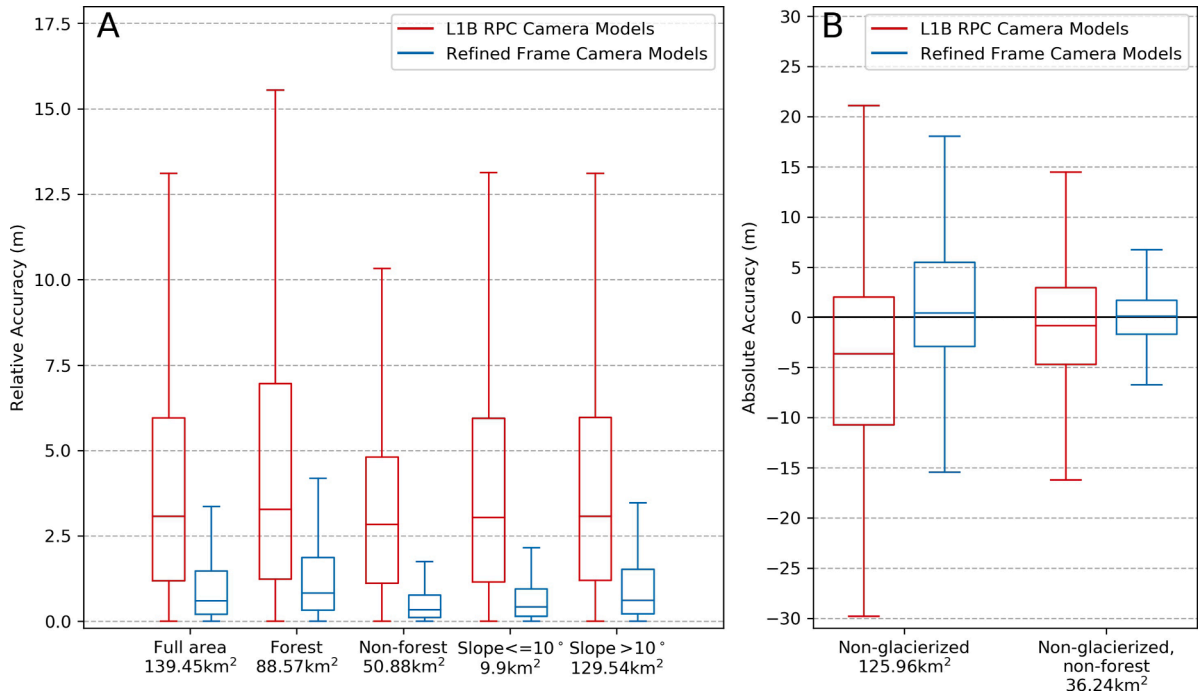

Fig. 6. Accuracy metrics using original L1B RPC camera models (red) and refined frame camera models (blue) for the Mt. Rainier SkySat triplet stereo case study. (A) Relative accuracy as represented by per-pixel NMAD values of the DEM composite (Fig. 5B, D) for different landcover and terrain classes, with respective areas. (B) Absolute accuracy as represented by elevation difference between the SkySat DEM composite and the reference LiDAR DEM (Fig. 5C, E) over static surfaces. Boxes show median and interquartile range, with whiskers at 1.5 times the interquartile range. (For interpretation of the references to colour in this figure legend, the reader is referred to the web version of this article.)

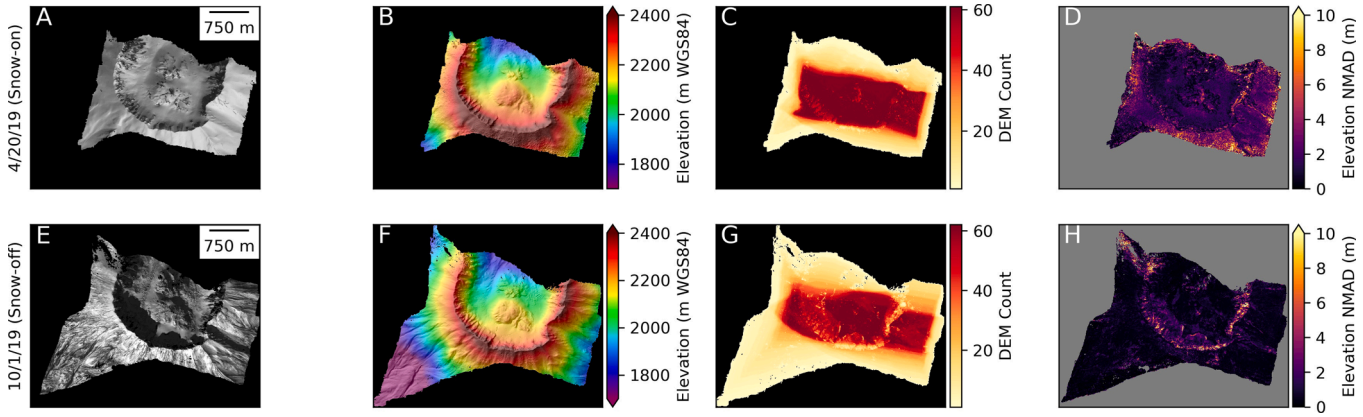

Fig. 7. SkySat video products for Mt. St. Helen's, acquired April 20, 2019 (near peak SWE, top row) and October 1, 2019 (near end of melt season, bottom row): (A,E) Orthoimage mosaic, (B,F) DEM composite from 62 stereo pairs, (C,G) per-pixel DEM count, and (D,H) per-pixel NMAD, which captures relative accuracy of the DEM composite. Note quality over steep crater walls and <1 m relative accuracy over crater floor and flanks. The orthoimage mosaics were derived from L1A imagery that is ©Planet, 2019.

two-view, and even triplet, stereo reconstruction due to occlusions.

Two 120-s SkySat videos were acquired for this study - one on April 20, 2019, near peak snow water equivalent (SWE) (hereafter, the "snow-on" collection) and the other on October 1, 2019, near the end of the summer snow/ice melt season ("snow-off" collection) (Fig. 7A, B). A light dusting of early-season snow was present on some surfaces during the October 1 video collection (Fig. 7B).

4.2.1. *Reference DEMs*

We used two reference DEMs derived from WorldView stereo images to process the SkySat video collections over Mt. St. Helen's - a summer reference DEM composite and a single spring reference DEM. The summer DEM composite (hereafter referred to as the "summer reference DEM") was generated from eight 2-m WorldView-1/2/3 DEMs acquired between 2013–2015 and co-registered to an airborne LiDAR DEM prior to compositing (Shean et al., 2016; Menounos et al., 2019). This summer reference DEM was used to initialize the frame camera models for both the snow-on and snow-off collections (Section 3.3), and to co-register the snow-off SkySat DEM over static surfaces (Section 3.7). Due to the limited availability of snow-free static surfaces within the small footprint of the snow-on SkySat DEM, we created the second reference DEM (hereafter referred to as the "spring reference DEM") from a WorldView-2 stereo pair acquired on April 28, 2019 (8 days after the snow-on SkySat video collection). To create this spring reference DEM, we used ASP with default MGM settings and then co-registered this spring reference DEM to the summer reference DEM over static surfaces distributed across the

much larger WorldView footprint (median difference of 0.09 m, NMAD of 0.86 m). The snow-on SkySat DEM composite was then co-registered to the spring reference DEM assuming that there was negligible elevation change during the eight day period.

4.2.2. Data processing

To evaluate the quality of the original, uncorrected SkySat video products, we ran our video processing workflow for both the snow-on and snow-off video collections using the original L1A RPC camera models without initial alignment orthorectification (Section 3.5). We then ran our full SkySat video processing workflow (Fig. 3B) using refined camera models.

Our default video processing workflow using an external reference DEM for the initial alignment orthorectification step worked well for most SkySat video samples (Fig. S4). The extreme relief of the St. Helen's crater and scale relative to the SkySat footprint, however, required an alternative strategy to avoid introducing artifacts that could lead to failed correlation and data gaps over the steep crater walls. The underlying issue is related to geolocation inconsistency between the L1A scenes and the external reference DEM, so we first generated a "smoothed initial DEM" from the original L1A scenes (Section 3.5, Fig. 3B) and and then used this DEM for initial alignment orthorectification, rather than the external reference DEM.

4.2.3. Results

Our workflow produced spatially continuous SkySat video DEM products with few data gaps, even over steep slopes on the crater walls (>40 to 50°). This is true for both the snow-on collect with limited surface texture over fresh snow (Fig. 7A), and the snow-off collect with shadows on north-facing slopes (Fig. 7E). The refined camera models from our workflow offer significantly improved relative DEM accuracy (Figs. 7D,H and 8A,B) compared to DEMs derived with the original RPC camera models (Fig. S6).

The snow-off DEM composite displays better relative accuracy than the snow-on DEM composite, with median per-pixel NMAD values of 0.45 and 1.64 m, respectively (8B). The larger per-pixel NMAD values for the snow-on DEM composite are indicative of residual camera inconsistencies after bundle adjustment, likely due to a reduced number of feature matches over snow. We also observe artifacts and larger per-pixel NMAD values of ~5 m in some areas of the snow-on DEM composite (Fig. 7D), likely due to erroneous disparities obtained during correlation over fresh snow with limited texture. The snow-off DEM composite also displays larger per-pixel NMAD values on northwest flank due to moving clouds during video collection (Fig. 7H).

The snow-on and snow-off DEM composites show limited absolute median bias (±NMAD) of 0.17 (±1.61) m and 0.30 (±1.83) m, respectively, compared to non-glacierized static surfaces in the corresponding spring and summer reference DEMs (Fig. 8C). These metrics provide estimates for the absolute accuracy of the SkySat DEMs, though some component of the observed residual elevation differences can be attributed to errors in the reference DEMs.

4.2.4. Elevation change from multiple SkySat DEMs

We computed elevation change for the ~5.5 month time-period (April 20 to October 1) by subtracting the co-registered snow-on DEM composite from the snow-off DEM composite (Fig. 9B). Relatively large negative elevation change signals are observed on the crater floor and within gullies/depressions on the flanks. Large negative signals are observed near the base of the western crater wall (green box in Fig. 9B). Limited elevation change is observed over the volcanic domes within the crater and ridges on the flanks.

The observed elevation change can be attributed to several processes. The negative elevation change over the crater floor and flanks can primarily be attributed to melting of relatively thick (>5–15 m) seasonal snowpack. The large negative signals within gullies and depressions on the flanks are indicative of preferential spring snow accumulation due to wind redistribution. Some of the observed elevation change over the Crater Glacier is also related to ice melt during summer, snow/firn compaction (e.g., Belart et al., 2017), and ice flow processes (e.g., Sold et al., 2013) including vertical submergence, advection of thickness anomalies, and crevasse opening/closing. The large elevation change values at the base of the western crater wall (green box in Fig. 9B) are likely related to melt of locally thick avalanche deposits present in the spring DEM and other local ice flow processes.

The near-zero elevation change over the volcanic domes can potentially be attributed to limited spring snow accumulation due to wind redistribution and/or increased geothermal heat flux causing continuous melting of snow during the accumulation season. The near-zero

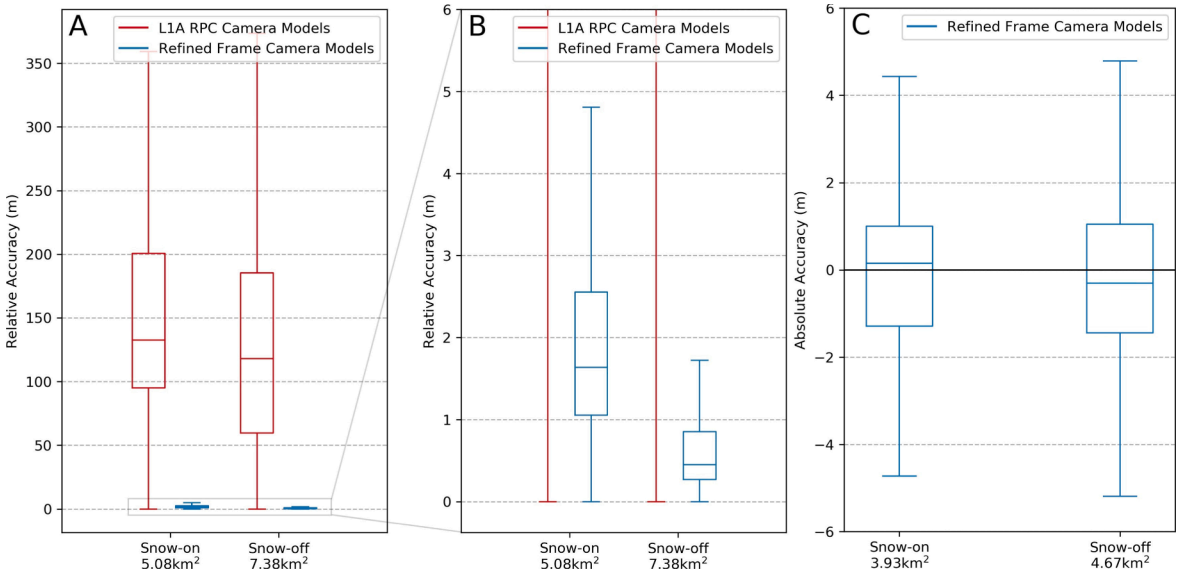

Fig. 8. Accuracy metrics using original L1A RPC camera models (red) and refined frame camera models (blue) for the Mt. St. Helen's SkySat video stereo case study. (A) Relative accuracy as represented by per-pixel NMAD values of the snow-on and snow-off DEM composites (Fig. 7D,H), with respective areas listed. (B) Same as in a (A), but zoomed to show detail of distribution for refined products. (C) Absolute accuracy as represented by elevation difference between the SkySat DEM composite and corresponding reference DEM over non-glacierized surfaces. Boxes show median and interquartile range, with whiskers at 1.5 times the interquartile range. (For interpretation of the references to colour in this figure legend, the reader is referred to the web version of this article.)

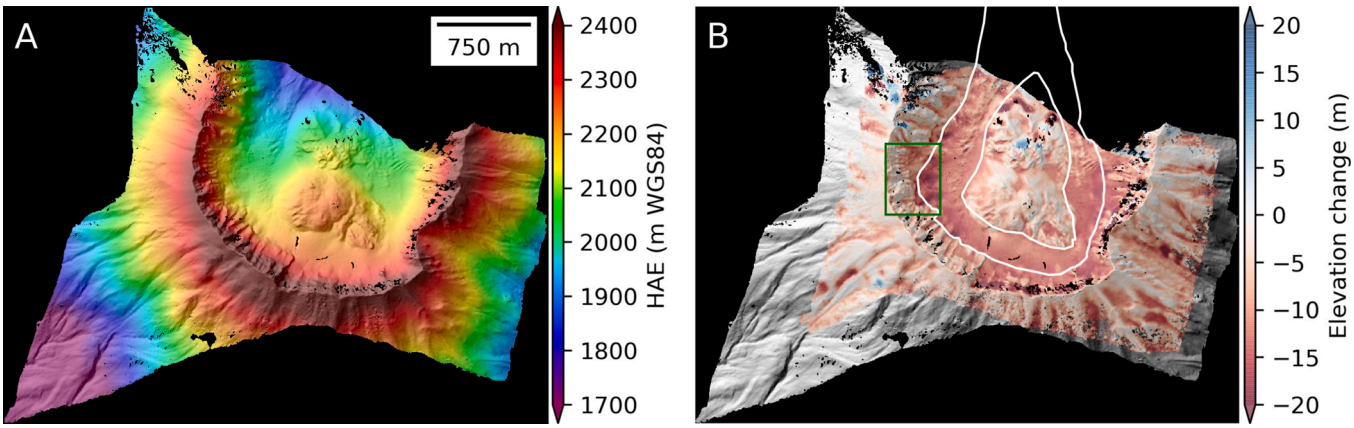

Fig. 9. (A) Mt. St. Helen's SkySat video DEM composite from October 1, 2019. (B) Elevation difference between the April 20, 2019 and October 1, 2019 DEM composites, documenting seasonal snow melt and other processes. White lines shows approximate Crater Glacier outline. Green box on west crater wall highlights large elevation change signals of ~10–20 m.

elevation change on the upper portion of the interior crater walls likely indicates limited or no snow accumulation in these areas, due to steep (>50°) surface slopes.

5. Discussion

We successfully generated high-quality DEM composites from the SkySat triplet stereo and video images. The bundled RPC models and L1A corner coordinates were not accurate enough to produce usable DEMs. This finding is consistent with those of previous geodetic studies involving products from Planet Dove (Ghuffar, 2018) and earlier SkySat sensors (d'Angelo et al., 2016). Our workflows correct these camera model issues to produce 2-m DEM composites with both high precision (<1 to 2 meter relative vertical accuracy, Figs. 6A and 8B) and accuracy (<2 to 3 m absolute vertical accuracy, Figs. 6B and 8C). Qualitatively, the 2-m DEM composites are able to resolve small-scale features such as narrow gullies and glacier crevasses at both of our study sites (Figs. 4 and 9).

5.1. SkySat triplet stereo evaluation

The per-pixel NMAD values for the Mt. Rainier triplet stereo DEM composite are slightly higher than the corresponding values for the video DEM composites, with larger residual offsets observed for scenes along the margins of the collection. This result can be attributed to two main causes. First, these marginal scenes mostly cover dense forests (Fig. 4), which are challenging for satellite stereo photogrammetry (e.g., Montesano et al., 2017, 2019; St-Onge and Grandin, 2019). Second, the scenes along the margins of a triplet collection have less overlap with neighboring scenes, and comparatively weaker connections during bundle adjustment.

The latter issue can potentially be corrected by individually co-registering each of the pairwise DEMs to a reference DEM after the bundle adjustment step, rather than creating a DEM composite and then co-registering. This alternative co-registration approach improved both the relative and absolute accuracy of the Mt. Rainier triplet stereo DEM products (Fig. S7). We attribute this success to the adequate distribution of both local topographic relief and static surfaces for all individual pairwise DEMs. However, this may not be the case for other sites with relatively flat or planar terrain, where some or all of the small pairwise SkySat DEMs may lack sufficient relief and/or static surface distribution. For this reason, our default workflow uses the DEM composite during the co-registration step, but the user can select the individual pairwise DEM co-registration strategy using the **`multi_align`** option in the **`skysat_pc_cam.py`** tool.

Some of these issues can also be addressed by exploiting the rigid relative orientation of the three detectors (Fig. 1), which should be consistent during the triplet stereo collection sequence. We explored this option by approximating a larger "virtual detector" combining three scenes acquired by the three detectors at a given timestamp, and accounting for the relative geometry of the three detectors in the SkySat focal plane. The resulting products included systematic artifacts and high triangulation errors indicative of residual detector geometry error. Beyond rigorous on-orbit geometric calibration of each SkySat-C using L1A images, it could be possible to improve our generic SkySat workflow by independently modeling each of the three detectors, but imposing constraints for their relative orientation during bundle adjustment.

5.2. SkySat video stereo evaluation

The limited per-pixel NMAD values for the SkySat video products indicate that the bundle adjustment step produced self-consistent camera models. We attribute this success to the high scene count and consistent, overlapping footprints of the SkySat video. When interpreting the absolute vertical accuracy of the Mt. St. Helen's video DEM composites, it is important to acknowledge the negative impact of both the limited distribution of static surfaces available for co-registration and the generally steep slopes within the crater, as the accuracy of both the SkySat and reference WorldView DEMs should be lower over steep terrain (e.g., Müller et al., 2014; Shean et al., 2016). We observe sub-meter absolute accuracy for a SkySat DEM composite produced from a similar symmetrical video collection over the relatively flat terrain over the Grand Mesa in Colorado, USA (Fig. S4A-D), compared to a reference WorldView DEM.

5.3. Limitations and considerations

As with any remote sensing technique, there are some limitations to consider when working with SkySat products.

5.3.1. Field of view

The individual SkySat scenes have a relatively small footprint (~2.5 km^2), with limited overlap between adjacent scenes (~10–15%) in the L1B mono collects. These limitations can lead to complications during several processing steps in our workflow. For instance, accurate feature matching over small overlapping ground footprints is difficult between scenes acquired from very different perspectives (e.g., larger convergence angles of ~ 27° to 55°), especially for steep terrain. Similarly, the small overlap between adjacent scenes results in weaker scene to scene connections during bundle adjustment (Section 3.4 and 5.1). These two issues are less relevant for the SkySat video products, as they have small perspective difference between scenes and high scene overlap

percentage (~95–100%). However, the small combined video footprint (~2.5 to 10 km^2), may have limited or no static surfaces available for co-registration (Section 3.7).

5.3.2. Surface texture

An essential component of any optical stereo photogrammetry workflow involves sparse and dense feature matching during bundle adjustment and image correlation, respectively. Given the relatively poor initial RPC geolocation accuracy for SkySat scenes, an initial bundle adjustment step is essential for subsequent stereo reconstruction. Feature matching success depends on adequate surface texture at spatial scales comparable to the native image GSD. For example, very high-resolution (VHR) imagery over urban areas should yield many unique features/keypoints, while VHR imagery over fresh snow on flat terrain may appear essentially featureless. A well-distributed set of sparse feature matches (i.e., not concentrated in one image corner) between overlapping images is essential to properly constrain the bundle adjustment optimization. For VHR satellite images with a large ground footprint (e.g., WorldView-2 swath width of 16.4 km), a well-distributed network of feature matches can usually be computed even if parts of the overlapping images have limited texture. However, the limited ground footprint of individual SkySat scenes can be problematic for feature matching, especially over surfaces with limited texture at ~1 m spatial scales (e.g., fresh snow). In such cases, a complete network of feature matches may not be constructed during bundle adjustment, due to limited correspondences between overlapping scenes. Similar problems can arise due to the presence of opaque clouds (e.g., Fig. 7E and S4M) and open water (e.g., Fig. S4Q). If poorly distributed feature matches are present near the more central, "anchor" scenes of a SkySat triplet stereo collect (i.e., regions with high DEM count in Fig. 5A), the bundle adjustment algorithm can introduce camera position and orientation error in adjacent scenes.

Even with perfectly calibrated camera models, erroneous disparities can pass stereo correlation filters, especially over surfaces with limited texture. Detector saturation over high-albedo surfaces can also result in failed correlation (e.g., Shean et al., 2016; Dai and Howat, 2018). Fortunately, our evaluation of SkySat products over multiple snow and ice targets (Fig. 4, 7, S3, S4) suggests that the 11-bit radiometric resolution, exposure cycling, and 0.9 m GSD of the SkySat products is generally sufficient to resolve small-scale features on most high-albedo snow and ice surfaces.

5.3.3. Reference DEM considerations

Our workflow requires a reference DEM during camera resection, initial alignment orthorectification, and 3D co-registration (Fig. 3). The choice of reference DEM is thus an important consideration, which depends on several factors. A reference DEM with high horizontal and vertical accuracy, limited sensor-dependent relative errors (e.g., variable radar penetration, LiDAR flightline offsets), complete overlap with the SkySat collection, limited data gaps, and limited time offset relative to the SkySat collection will produce better results during all processing steps. Additionally, if possible, the GSD of the reference DEM should be less than or approximately equal to that of the SkySat DEM composite to improve absolute geolocation accuracy during ICP co-registration.

Where available, we recommend using a reference DEM derived from airborne laser scanning (LiDAR) or other very-high-resolution stereo satellite imagery (e.g., DigitalGlobe/Maxar WorldView-3) that has been corrected with accurate control data. Alternatively, as demonstrated in Section 4.1.3, high-quality SkySat DEMs can also be generated using publicly available reference DEMs with limited resolution and accuracy (e.g., SRTM, NED). Furthermore, if the intended use case is to measure relative elevation change between the SkySat DEM and a reference DEM, then the absolute geolocation accuracy of the reference DEM is less relevant, as relative offsets between the two will be minimized during co-registration.

It is interesting to note that the snow-on SkySat DEM composite has better apparent absolute accuracy than the snow-off SkySat DEM composite (Fig. 8C). This might be attributed to the more limited time interval (8 days) between the snow-on SkySat DEM and spring reference DEM, with minimal expected surface elevation change over surfaces assumed to be static. In contrast, the snow-off SkySat DEM and the corresponding summer reference DEM composite are separated by several years, and some surfaces assumed to be static likely changed (e.g., mass wasting over steep crater walls), leading to an apparent decrease in SkySat DEM accuracy.

The better apparent absolute accuracy of snow-on DEM composite may also be a direct consequence of the relatively smooth, snow-covered surface. Thick snow will fill small gullies, cover small ridges, and accumulate at the base of steep slopes, all serving to reduce surface roughness. This reduced small-scale roughness may be slightly more forgiving of any reduction in DEM resolving power due to residual camera alignment issues and "blurring" during pairwise DEM compositing.

5.4. Multi-view triangulation

Our default workflow uses a pairwise (two-view) stereo triangulation strategy for multiple image pairs, instead of using true multi-view triangulation for all images. Based on previous tests, we hypothesized that the quality of the per-pixel median composite from all pairwise DEMs would match or potentially exceed the quality of DEM products produced using multi-view triangulation. We tested an experimental multi-view stereo implementation for the SkySat video collections (Sections 3.2.3, 3.5). The resulting multi-view DEM composites contain more noise than the pairwise DEM composites, with visible seam boundaries (Fig. S8). This result is consistent with those from previous studies suggesting that a DEM composite derived from many self-consistent pairwise DEMs (e.g., Ozcanli et al., 2016) is able to resolve more detail with better signal-to-noise ratio than a DEM obtained by conventional multi-view implementations (e.g., Facciolo et al., 2017). This limitation can potentially be improved by assigning increased weight to pairs with larger convergence angles (and reduced uncertainty) during multi-view triangulation (Delon and Rougé, 2007).

5.5. Structure from motion

To further explore multi-view triangulation options, we attempted to process SkySat video and triplet stereo datasets using two commercial SfM packages, Pix4DMapper and Agisoft Metashape, and one open-source package, COLMAP (Schönberger et al., 2016; Schönberger and Frahm, 2016).

We found that the initial bundle adjustment step for these packages was relatively unstable for SkySat scenes. When solving for both extrinsics and intrinsics, multiple runs with identical input images and settings produced different solutions. When solving for extrinsics only, both COLMAP and Pix4DMapper provided reasonable solutions for the snow-on Mt. St. Helen's video dataset, but neither package successfully refined all cameras for the Mt. Rainier triplet stereo dataset.

One possible path forward might involve initial camera resection and bundle adjustment with our workflow, followed by dense reconstruction and multi-view triangulation with one of these SfM packages (e.g., Zhang et al., 2019). Future analysis will allow for more detailed evaluation of our pairwise stereo DEM composites vs. SfM multi-view stereo DEM products.

6. Conclusions and summary

The SkySat-C constellation offers new potential for on-demand, large-scale, 3D mapping of the Earth's surface, with relatively limited tasking competition, short repeat imaging interval, and low cost. The ~100 km^2 ground footprint of the SkySat triplet stereo products and area tasking strategy has the potential for systematic 3D reconstruction

of larger areas over a short time window. The SkySat video products cover a more limited ~2.5 to 10 km^2 area, but they can be used for multi-view stereo reconstruction over sites which are challenging for two-image or triplet stereo (e.g., steep mountains and dense vegetation). However, the accuracy of the resulting DEM products is limited by the relatively poor geolocation accuracy of the original Level-1A/1B SkySat camera models and inconsistent orientation of individual scenes in both the collects and videos. As a result of these limitations, and the absence of robust processing software, SkySat imagery has not yet seen widespread use for stereo reconstruction.

We developed an automated, open-source workflow to refine the SkySat camera models and improve absolute geolocation accuracy using external reference DEMs, without manual GCP selection. These refined camera models are then used to produce accurate, self-consistent DEM and orthoimage composites from both the SkySat triplet stereo and video products.

We found that pairwise triangulation followed by compositing produced better output products with more detail and less noise than true multi-view triangulation. We also obtained comparable relative accuracy for SkySat DEM composites produced using both a 1-m LiDAR DSM and the 30-m SRTM-GL1 as reference DEMs, confirming that high-quality SkySat DEMs can be produced on a global scale using publicly available coarse-resolution reference DEMs like SRTM.

The small overlap (~10%) between adjacent L1B scenes in each SkySat triplet stereo collect can cause issues during bundle adjustment. We were able to mitigate these issues by co-registering individual pairwise DEMs to a reference DEM, rather than the full DEM composite. This strategy may work for sites with adequate relief and static surface distribution, but may fail for planar surfaces. Future availability of L1A scenes with greater scene-to-scene overlap (~90%) and additional camera position metadata should offer new opportunities to constrain the triplet stereo bundle adjustment optimization and improve stereo reconstruction results.

We presented case studies for SkySat stereo samples collected over Mt. Rainier and Mt. St. Helen's, which include terrain and landcover that is challenging for stereo reconstruction. The output DEM composites have <1 to 2 m relative and <2 to 3 m absolute vertical accuracy compared to reference airborne LiDAR and WorldView stereo DEMs, with highest accuracy over vegetation-free surfaces and limited surface slopes. Qualitatively, the output 2-m SkySat DEMs have few data gaps and are able to resolve small-scale surface features such as narrow gullies and glacier crevasses. We also computed elevation difference between two repeat SkySat video DEM composites over Mt. St. Helen's, collected during spring (peak snow extent/depth) and late summer (minimum snow extent/depth). These products document total snow depth of ~5–15 m and other elevation change due to avalanches and glacier flow.

The methods presented here can be applied to other frame camera imaging systems, including those on planetary orbiters (e.g., Edwards et al., 2005; Edwards and Broxton, 2006), aerial/UAV platforms (e.g., Knuth et al., 2020; Alexandrov, 2017; Meyer and Skiles, 2019), and the Planet Doves. We hope to improve our current workflow with additional bundle adjustment constraints, better multi-view stereo triangulation approaches, and more sophisticated point cloud processing. We are also working to produce improved landcover classification products derived from contemporaneous SkySat multispectral imagery at native resolution for use during co-registration (e.g., Deschamps-Berger et al., 2020; Hu and Shean, 2020). Finally, we will continue to improve the open-source code accompanying this manuscript, and hope to scale processing efforts to study the Earth's evolving surface on a regional to global scale using the growing SkySat stereo archive.

Funding

This research was supported by the NASA Terrestrial Hydrology Program (THP) and the NASA Cryosphere Program. SB was supported by a NASA FINESST award (80NSSC19K1338) and the NASA HiMAT project (NNX16AQ88G). DS, OA and SH were supported by NASA THP award 80NSSC18K1405. Tasking, data access, and supplemental support was provided by the NASA Commercial Smallsat Data Acquisition Program 2018 Pilot Study.

Author contributions

Shashank Bhushan led the study, developed processing workflows with input from all co-authors, processed data, generated figures and wrote the first draft of the manuscript with David Shean. David Shean managed the project, acquired funding, provided guidance on methodology, and essential support in manuscript development, organisation and writing. Oleg Alexandrov led the modification of the ASP codebase to support SkySat sensors and provided valuable insight on photogrammetry theory and workflows. Scott Henderson documented initial issues with SkySat metadata and performed initial video processing experiments. All authors contributed to the final version of the manuscript.

Declaration of Competing Interest

The authors declare the following financial interests/personal relationships which may be considered as potential competing interests: [Shashank Bhushan participated in a 10-week internship program at Planet during summer 2020. All software development, data processing, analysis and manuscript preparation (before revision) was completed before the internship.]

Acknowledgements

We acknowledge Compton J. Tucker and others at NASA Goddard Space Flight Center and NASA Headquarters for coordinating the Commercial Smallsat Data Acquisition Program Pilot and assisting with preliminary SkySat tasking campaigns. Paris Good at Planet provided invaluable assistance with data acquisition and facilitated discussions with Planet engineering teams. Thanks are also due to Ross Losher, Antonio Martos, Kelsey Jordahl and others at Planet for initial guidance on SkySat-C sensor specifications and camera models. Resources supporting this work were provided by the NASA High-End Computing (HEC) Program through the NASA Advanced Supercomputing (NAS) Division at Ames Research Center. The Maxar WorldView L1B stereo imagery used to generate reference DEMs was available under the NGA NextView/EnhancedView license. Friedrich Knuth and Michelle Hu provided feedback on initial manuscript outline and code development. Eric Gagliano assisted in latex formatting. We thank two anonymous reviewers for providing valuable and constructive input that significantly improved the quality of this manuscript. We also acknowledge input from the larger ASP community during photogrammetry discussions.

Appendix A. Supplementary material

Supplementary data associated with this article can be found, in the online version, at https://doi.org/10.1016/j.isprsjprs.2020.12.012.

References

Albino, F., Smets, B., d'Oreye, N., Kervyn, F., 2015. High-resolution TanDEM-X DEM: An accurate method to estimate lava flow volumes at Nyamulagira Volcano (D. R. Congo): TANDEM-X DEM TO DERIVE LAVA FLOW VOLUMES. J. Geophys. Res.: Solid Earth 120, 4189–4207. https://doi.org/10.1002/2015JB011988. http://doi.wiley.com/10.1002/2015JB011988.

Alexandrov, O., 2017. IceBridge DMS L3 Ames Stereo Pipeline Photogrammetric DEM, Version 1. https://nsidc.org/data/IODEM3/versions/1, doi:10.5067/HYV1T0G7LVHE. type: dataset.

Amer, F., 2006. Digital block adjustment. Photogram. Rec. 4, 34–49. https://doi.org/10.1111/j.1477-9730.1962.tb00324.x. http://doi.wiley.com/10.1111/j.1477-9730.1962.tb00324.x.

Belart, J.M.C., Berthier, E., Magnússon, E., Anderson, L.S., Pálsson, F., Thorsteinsson, T., Howat, I.M., Aðalgeirsdóttir, G., Jóhannesson, T., Jarosch, A.H., 2017. Winter mass balance of Drangajökull ice cap (NW Iceland) derived from satellite sub-meter stereo images. Cryosphere 11, 1501–1517. https://doi.org/10.5194/tc-11-1501-2017. https://www.the-cryosphere.net/11/1501/2017/.

Beyer, R., Alexandrov, O., ScottMcMichael, Broxton, M., Lundy, M., Husmann, K., Edwards, L., Nefian, A., SmithB, Shean, D., Smith, T., mstyer, Annex, A., Moratto, Z., harguess, Aravkin, A., Meyer, J., Bhushan, S., jlaura, 2020. Neogeographytoolkit/stereopipeline 2.7.0. doi: 10.5281/zenodo.3963341.

Beyer, R.A., Alexandrov, O., McMichael, S., 2018. The Ames Stereo Pipeline: NASA's Open Source Software for Deriving and Processing Terrain Data. Earth Space Sci. 5, 537–548. https://doi.org/10.1029/2018EA000409. http://doi.wiley.com/10.1029/2018EA000409.

Bhushan, S., Shean, D., Alexandrov, O., Henderson, S., 2021. uw-cryo/skysat_stereo: Zenodo doi revision updates. https://github.com/uw-cryo/skysat_stereo. doi: 10.5281/zenodo.4422248.

Brun, F., Berthier, E., Wagnon, P., Kääb, A., Treichler, D., 2017. A spatially resolved estimate of High Mountain Asia glacier mass balances from 2000 to 2016. Nat. Geosci. 10, 668–673. https://doi.org/10.1038/ngeo2999. http://www.nature.com/doifinder/10.1038/ngeo2999.

Brun, F., Wagnon, P., Berthier, E., Shea, J.M., Immerzeel, W.W., Kraaijenbrink, P.D.A., Vincent, C., Reverchon, C., Shrestha, D., Arnaud, Y., 2018. Ice cliff contribution to the tongue-wide ablation of Changri Nup Glacier, Nepal, central Himalaya. Cryosphere 12, 3439–3457. https://doi.org/10.5194/tc-12-3439-2018. https://www.the-cryosphere.net/12/3439/2018/.

Büyüksalih, G., Jacobsen, K., 2006. Generation and validation of digital elevation models based on satellite images, 6.

Christopherson, J., Ramaseri Chandra, S., Quanbeck, J., 2019. 2019 Joint Agency Commercial Imagery Evaluation—Land remote sensing satellite compendium: U.S. Geological Survey Circular 1455. Technical Report. doi:doi.org/10.3133/cir1455.

Dai, C., Durand, M., Howat, I.M., Altenau, E.H., Pavelsky, T.M., 2018. Estimating River Surface Elevation From ArcticDEM. Geophys. Res. Lett. 45, 3107–3114. https://doi.org/10.1002/2018GL077379. https://onlinelibrary.wiley.com/doi/abs/10.1002/2018GL077379.

Dai, C., Howat, I.M., 2018. Detection of saturation in high-resolution Pushbroom satellite imagery. IEEE J. Sel. Top. Appl. Earth Observ. Remote Sens. 11, 1684–1693. https://doi.org/10.1109/JSTARS.2018.2814543.

d'Angelo, P., Kuschk, G., 2012. Dense multi-view stereo from satellite imagery. In: 2012 IEEE International Geoscience and Remote Sensing Symposium. IEEE, Munich, Germany, pp. 6944–6947. https://doi.org/10.1109/IGARSS.2012.6352565. http://ieeexplore.ieee.org/document/6352565/.

d'Angelo, P., Máttyus, G., Reinartz, P., 2016. Skybox image and video product evaluation. Int. J. Image Data Fusion 7, 3–18. https://doi.org/10.1080/19479832.2015.1109565. http://www.tandfonline.com/doi/full/10.1080/19479832.2015.1109565.

d'Angelo, P., Reinartz, P., 2012. Dsm based orientation of large stereo satellite image blocks. ISPRS – Int. Arch. Photogramm. Remote Sens. Spatial Inf. Sci. XXXIX-B1, 209–214. https://doi.org/10.5194/isprsarchives-XXXIX-B1-209-2012. https://www.int-arch-photogramm-remote-sens-spatial-inf-sci.net/XXXIX-B1/209/2012/.

Dehecq, A., Gardner, A.S., Alexandrov, O., McMichael, S., Hugonnet, R., Shean, D., Marty, M., 2020. Automated processing of declassified KH-9 hexagon satellite images for global elevation change analysis since the 1970s. frontiers. Earth Sci. 8, 566802. https://doi.org/10.3389/feart.2020.566802. https://www.frontiersin.org/articles/10.3389/feart.2020.566802/full.

Deilami, K., Hashim, M., 2011. Very high resolution optical satellites for DEM generation: a review. Eur. J. Sci. Res. 49, 14.

Delon, J., Rougé, B., 2007. Small baseline stereovision. J. Math. Imaging Vision 28, 209–223. https://doi.org/10.1007/s10851-007-0001-1. http://link.springer.com/10.1007/s10851-007-0001-1.

Deschamps-Berger, C., Gascoin, S., Berthier, E., Deems, J., Gutmann, E., Dehecq, A., Shean, D., Dumont, M., 2020. Snow depth mapping from stereo satellite imagery in mountainous terrain: evaluation using airborne laser-scanning data. Cryosphere 14, 2925–2940. https://doi.org/10.5194/tc-14-2925-2020. https://tc.copernicus.org/articles/14/2925/2020/.

Dewitz, J., 2019. National Land Cover Dataset (NLCD) 2016 Products. https://www.sciencebase.gov/catalog/item/5d4c6a1de4b01d82ce8dfd2f, doi:10.5066/P96HHBIE. type: dataset.

DigitalGlobe, 2016. Accuracy of worldview products. https://dg-cms-uploads-production.s3.amazonaws.com/uploads/document/file/38/DG_ACCURACY_WP_V3.pdf. last accessed 30 May 2020.

Edwards, L., Broxton, M., 2006. Automated 3D Surface Reconstruction from Orbital Imagery. In: Space 2006. American Institute of Aeronautics and Astronautics, San Jose, California. https://doi.org/10.2514/6.2006-7435. http://arc.aiaa.org/doi/10.2514/6.2006-7435.

Edwards, L., Sims, M., Kunz, C., Lees, D., Bowman, J., 2005. Photo-realistic terrain modeling and visualization for mars exploration rover science operations. In: 2005 IEEE International Conference on Systems, Man and Cybernetics. IEEE, Waikoloa, HI, USA, pp. 1389–1395. https://doi.org/10.1109/ICSMC.2005.1571341.

Facciolo, G., De Franchis, C., Meinhardt-Llopis, E., 2017. Automatic 3d reconstruction from multi-date satellite images. In: 2017 IEEE Conference on Computer Vision and Pattern Recognition Workshops (CVPRW), pp. 1542–1551.

Facciolo, G., Franchis, C.d., Meinhardt, E., 2015. MGM: A significantly more global matching for stereovision. In: Procedings of the British Machine Vision Conference 2015. British Machine Vision Association, Swansea, pp. 90.1–90.12. https://doi.org/10.5244/C.29.90.

Farr, T.G., Rosen, P.A., Caro, E., Crippen, R., Duren, R., Hensley, S., Kobrick, M., Paller, M., Rodriguez, E., Roth, L., Seal, D., Shaffer, S., Shimada, J., Umland, J., Werner, M., Oskin, M., Burbank, D., Alsdorf, D., 2007. The shuttle radar topography mission. Rev. Geophys. 45, RG2004. https://doi.org/10.1029/2005RG000183.

de Franchis, C., Meinhardt-Llopis, E., Michel, J., Morel, J.M., Facciolo, G., 2014. An automatic and modular stereo pipeline for pushbroom images. ISPRS Anna. Photogramm. Remote Sens. Spatial Inf. Sci. II-3, 49–56. https://doi.org/10.5194/isprsannals-II-3-49-2014.

Ghuffar, S., 2018. DEM generation from multi satellite PlanetScope imagery. Remote Sens. 10, 1462. https://doi.org/10.3390/rs10091462.

Höhle, J., Höhle, M., 2009. Accuracy assessment of digital elevation models by means of robust statistical methods. ISPRS J. Photogramm. Remote Sens. 64, 398–406. https://doi.org/10.1016/j.isprsjprs.2009.02.003. https://linkinghub.elsevier.com/retrieve/pii/S0924271609000276.

Howat, I.M., Porter, C., Smith, B.E., Noh, M.J., Morin, P., 2019. The reference elevation model of antarctica. Cryosphere 13, 665–674. https://doi.org/10.5194/tc-13-665-2019. https://tc.copernicus.org/articles/13/665/2019/.

Hu, M., Shean, D., 2020. Machine learning classification and derived snow metrics from very-high-resolution multispectral satellite imagery in complex terrain. Hydrology. https://doi.org/10.1002/essoar.10501632.1. http://www.essoar.org/doi/10.1002/essoar.10501632.1.

Kehrl, L.M., Joughin, I., Shean, D.E., Floricioiu, D., Krieger, L., 2017. Seasonal and interannual variabilities in terminus position, glacier velocity, and surface elevation at Helheim and Kangerlussuaq Glaciers from 2008 to 2016: Helheim and Kangerlussuaq Glaciers. J. Geophys. Res.: Earth Surf. 122, 1635–1652. https://doi.org/10.1002/2016JF004133. http://doi.wiley.com/10.1002/2016JF004133.

Kellndorfer, J., Walker, W., Pierce, L., Dobson, C., Fites, J.A., Hunsaker, C., Vona, J., Clutter, M., 2004. Vegetation height estimation from Shuttle Radar Topography Mission and National Elevation Datasets. Remote Sens. Environ. 93, 339–358. https://doi.org/10.1016/j.rse.2004.07.017. https://linkinghub.elsevier.com/retrieve/pii/S0034425704002330.

Kennedy, L.A., Russell, J.K., 2012. Cataclastic production of volcanic ash at Mount Saint Helens. Phys. Chem. Earth Parts A/B/C 45–46, 40–49. https://doi.org/10.1016/j.pce.2011.07.052. https://linkinghub.elsevier.com/retrieve/pii/S1474706511001689.

Kim, J.W., Lu, Z., Qu, F., Hu, X., 2015. Pre-2014 mudslides at Oso revealed by InSAR and multi-source DEM analysis. Geomatics, Natural Hazards Risk 6, 184–194. https://doi.org/10.1080/19475705.2015.1016556. http://www.tandfonline.com/doi/abs/10.1080/19475705.2015.1016556.

Knuth, F., Shean, D., Alexandrov, O., Bhushan, S., 2020. Automated production of high-resolution DEMs from historical imagery for quantitative analysis of glacier and geomorphological change. other. Hydrology. https://doi.org/10.1002/essoar.10501805.1. http://www.essoar.org/doi/10.1002/essoar.10501805.1.

Leotta, M.J., Long, C., Jacquet, B., Zins, M., Lipsa, D., Shan, J., Xu, B., Li, Z., Zhang, X., Chang, S.F., Purri, M., Xue, J., Dana, K., 2019. Urban semantic 3D reconstruction from multiview satellite imagery. In: 2019 IEEE/CVF Conference on Computer Vision and Pattern Recognition Workshops (CVPRW). IEEE, Long Beach, CA, USA, pp. 1451–1460. https://doi.org/10.1109/CVPRW.2019.00186. https://ieeexplore.ieee.org/document/9025699/.

Marí, R., de Franchis, C., Meinhardt-Llopis, E., Facciolo, G., 2019. To bundle adjust or not: a comparison of relative geolocation correction strategies for satellite multi-view stereo. In: 2019 IEEE/CVF International Conference on Computer Vision Workshop (ICCVW), pp. 2188–2196. https://doi.org/10.1109/ICCVW.2019.00274.

Marta, S., 2019. Planet Imagery Product Specifications. https://assets.planet.com/docs/combined-imagery-product-spec-final-august-2019.pdf. last accessed 30 May 2020.

Menounos, B., Hugonnet, R., Shean, D., Gardner, A., Howat, I., Berthier, E., Pelto, B., Tennant, C., Shea, J., Noh, M., Brun, F., Dehecq, A., 2019. Heterogeneous changes in Western North American glaciers linked to decadal variability in zonal wind strength. Geophys. Res. Lett. 46, 200–209. https://doi.org/10.1029/2018GL080942. https://onlinelibrary.wiley.com/doi/abs/10.1029/2018GL080942.

Meyer, J., Skiles, S.M., 2019. Assessing the ability of structure from motion to map high-resolution snow surface elevations in complex terrain: a case study From Senator Beck Basin, CO. Water Resour. Res. 55, 6596–6605. https://doi.org/10.1029/2018WR024518. https://agupubs.onlinelibrary.wiley.com/doi/abs/10.1029/2018WR024518.

Mikhail, E.M., Bethel, J.S., McGlone, J.C., 2001. Introduction to modern photogrammetry. Wiley, New York: Chichester. OCLC: ocm45735791.

Müller, J., Gärtner-Roer, I., Thee, P., Ginzler, C., 2014. Accuracy assessment of airborne photogrammetrically derived high-resolution digital elevation models in a high mountain environment. ISPRS J. Photogramm. Remote Sens. 98, 58–69. https://doi.org/10.1016/j.isprsjprs.2014.09.015. https://linkinghub.elsevier.com/retrieve/pii/S0924271614002408.

Montesano, P.M., Neigh, C., Sun, G., Duncanson, L., Van Den Hoek, J., Ranson, K.J., 2017. The use of sun elevation angle for stereogrammetric boreal forest height in open canopies. Remote Sens. Environ. 196, 76–88. https://doi.org/10.1016/j.rse.2017.04.024. https://linkinghub.elsevier.com/retrieve/pii/S0034425717301827.

Montesano, P.M., Neigh, C.S., Wagner, W., Wooten, M., Cook, B.D., 2019. Boreal canopy surfaces from spaceborne stereogrammetry. Remote Sens. Environ. 225, 148–159. https://doi.org/10.1016/j.rse.2019.02.012. https://linkinghub.elsevier.com/retrieve/pii/S0034425719300677.

Morrison, R.A., Turner, J.T., Barwick, M., Hardaway, G.M., 2005. Urban reconnaissance with an airborne laser radar (Invited Paper), Orlando, Florida, USA. p. 1. http://proceedings.spiedigitallibrary.org/proceeding.aspx?doi=10.1117/12.609675, doi:10.1117/12.609675.

NASA Earth Science Division, 2020. Commercial SmallSat Data Acquisition Program Pilot Evaluation Report. Technical Report. NASA Earth Science Division. https://cdn.earthdata.nasa.gov/conduit/upload/14180/CSDAPEvaluationReport_Apr20.pdf. last accessed 30 October 2020.

NASA Shuttle Radar Topography Mission (SRTM), 2013. Shuttle Radar Topography Mission (SRTM) Global. https://portal.opentopography.org/raster?opentopoID=OTSRTM.082016.4326.1, 2020, doi:10.5069/G9445JDF. distributed by OpenTopography. Last accessed 5 November.

Nefian, A.V., Husmann, K., Broxton, M., To, V., Lundy, M., Hancher, M.D., 2009. A bayesian formulation for sub-pixel refinement in stereo orbital imagery.

Noh, M.J., Howat, I.M., 2015. Automated stereo-photogrammetric DEM generation at high latitudes: Surface Extraction with TIN-based Search-space Minimization (SETSM) validation and demonstration over glaciated regions. GIScience Remote Sens. 52, 198–217. https://doi.org/10.1080/15481603.2015.1008621. http://www.tandfonline.com/doi/full/10.1080/15481603.2015.1008621.

Ozcanli, O.C., Dong, Y., Mundy, J.L., Webb, H., Hammoud, R., Tom, V., 2016. Automatic geolocation correction of satellite imagery. Int. J. Comput. Vision 116, 263–277. https://doi.org/10.1007/s11263-015-0852-7. http://link.springer.com/10.1007/s11263-015-0852-7.

Piermattei, L., Marty, M., Karel, W., Ressl, C., Hollaus, M., Ginzler, C., Pfeifer, N., 2018. Impact of the acquisition geometry of very high-resolution Pléiades imagery on the accuracy of canopy height models over forested alpine regions. Remote Sens. 10, 1542. https://doi.org/10.3390/rs10101542. http://www.mdpi.com/2072-4292/10/10/1542.

Pomerleau, F., Colas, F., Siegwart, R., Magnenat, S., 2013. Comparing ICP variants on real-world data sets: open-source library and experimental protocol. Autonom. Robots 34, 133–148. https://doi.org/10.1007/s10514-013-9327-2. http://link.springer.com/10.1007/s10514-013-9327-2.

Porter, C., Morin, P., Howat, I., Noh, M.J., Bates, B., Peterman, K., Keesey, S., Schlenk, M., Gardiner, J., Tomko, K., Willis, M., Kelleher, C., Cloutier, M., Husby, E., Foga, S., Nakamura, H., Platson, M., Wethington, M., Williamson, C., Bauer, G., Enos, J., Arnold, G., Kramer, W., Becker, P., Doshi, A., D'Souza, C., Cummens, P., Laurier, F., Bojesen, M., 2018. ArcticDEM. https://dataverse.harvard.edu/citation?persistentId=doi:10.7910/DVN/OHHUKH, doi:10.7910/DVN/OHHUKH. type: dataset.

RGI Consortium, 2017. Randolph Glacier Inventory – A Dataset of Global Glacier Outlines: Version 6.0: Technical Report. Technical Report. Global Land Ice Measurements from Space, Colorado, USA. Digital Media. doi:10.7265/N5-RGI-60.

Robinson, J.E., S.T., Swinney, D., 2010. Digital topographic map showing the extents of glacial ice and perennial snowfields at mount rainier, washington, based on the lidar survey of september 2007 to october 2008. https://pubs.usgs.gov/ds/549/.

Rounce, D.R., King, O., McCarthy, M., Shean, D.E., Salerno, F., 2018. Quantifying debris thickness of debris-covered glaciers in the everest region of nepal through inversion of a subdebris melt model. J. Geophys. Res.: Earth Surf. 123, 1094–1115. https://doi.org/10.1029/2017JF004395. http://doi.wiley.com/10.1029/2017JF004395.

Schilling, S.P., Carrara, P.E., Thompson, R.A., Iwatsubo, E.Y., 2004. Posteruption glacier development within the crater of Mount St. Helens, Washington, USA. Quaternary Res. 61, 325–329. https://www.cambridge.org/core/product/identifier/S003358940001303X/type/journal_article, doi:10.1016/j.yqres.2003.11.002.

Schönberger, J.L., Frahm, J.M., 2016. Structure-from-motion revisited. In: Conference on Computer Vision and Pattern Recognition (CVPR).

Schönberger, J.L., Zheng, E., Pollefeys, M., Frahm, J.M., 2016. Pixelwise view selection for unstructured multi-view stereo. In: European Conference on Computer Vision (ECCV).

Shean, D., Bhushan, S., Lilien, D., Meyer, J., 2019. dshean/demcoreg: Zenodo doi release. https://github.com/dshean/demcoreg, doi:10.5281/zenodo.3243481.

Shean, D.E., Alexandrov, O., Moratto, Z.M., Smith, B.E., Joughin, I.R., Porter, C., Morin, P., 2016. An automated, open-source pipeline for mass production of digital elevation models (DEMs) from very-high-resolution commercial stereo satellite imagery. ISPRS J. Photogramm. Remote Sens. 116, 101–117. https://doi.org/10.1016/j.isprsjprs.2016.03.012. https://linkinghub.elsevier.com/retrieve/pii/S0924271616300107.

Shean, D.E., Bhushan, S., Montesano, P., Rounce, D.R., Arendt, A., Osmanoglu, B., 2020. A systematic, regional assessment of high mountain asia glacier mass balance. Front. Earth Sci. 7, 363. https://doi.org/10.3389/feart.2019.00363. https://www.frontiersin.org/article/10.3389/feart.2019.00363/full.

Sisson, T., Robinson, J., Swinney, D., 2011. Whole-edifice ice volume change A.D. 1970 to 2007/2008 at Mount Rainier, Washington, based on LiDAR surveying. Geology 39, 639–642. https://doi.org/10.1130/G31902.1 arXiv:https://pubs.geoscienceworld.org/geology/article-pdf/39/7/639/3540733/639.pdf.

Slabaugh, G., Schafer, R., Livingston, M., 2001. Optimal ray intersection for computing 3d points from n-view correspondences. http://gregslabaugh.net/publications/opray.pdf.

Sold, L., Huss, M., Hoelzle, M., Andereggen, H., Joerg, P.C., Zemp, M., 2013. Methodological approaches to infer end-of-winter snow distribution on alpine glaciers. J. Glaciol. 59, 1047–1059. https://doi.org/10.3189/2013JoG13J015. https://www.cambridge.org/core/product/identifier/S0022143000203766/type/journal_article.

St-Onge, B., Grandin, S., 2019. Estimating the height and basal area at individual tree and plot levels in canadian subarctic lichen woodlands using stereo worldview-3 images. Remote Sens. 11, 248. https://doi.org/10.3390/rs11030248. http://www.mdpi.com/2072-4292/11/3/248.

Tian, J., Reinartz, P., D'angelo, P., 2012. Change detection analysis of forest areas using satellite stereo data. In: Clasen, M., Fröhlich, G., Bernhardt, H., Hildebrand, K., Theuvsen, B. (Eds.), Informationstechnologie für eine nachhaltige Landbewirtschaftung – Fokus: Forstwirtschaft, Gesellschaft für Informatik e.V., Bonn. pp. 311–314.

Triggs, B., McLauchlan, P.F., Hartley, R.I., Fitzgibbon, A.W., 2000. Bundle Adjustment — A Modern Synthesis. In: Goos, G., Hartmanis, J., van Leeuwen, J., Triggs, B., Zisserman, A., Szeliski, R. (Eds.), Vision Algorithms: Theory and Practice, vol. 1883. Springer, Berlin, Heidelberg, pp. 298–372. https://doi.org/10.1007/3-540-44480-7_21. http://link.springer.com/10.1007/3-540-44480-7_21.

Wan, X., Liu, J., Yan, H., Morgan, G.L., Sun, T., 2016. 3D super resolution scene depth reconstruction based on SkySat video image sequences. In: 2016 IEEE International Geoscience and Remote Sensing Symposium (IGARSS). IEEE, Beijing, China, pp. 6653–6656. https://doi.org/10.1109/IGARSS.2016.7730737. http://ieeexplore.ieee.org/document/7730737/.

Willis, M.J., Herried, B.G., Bevis, M.G., Bell, R.E., 2015. Recharge of a subglacial lake by surface meltwater in northeast Greenland. Nature 518, 223–227. https://doi.org/10.1038/nature14116. http://www.nature.com/articles/nature14116.

Zhai, C., Dyer, J., Lu, E., Buie, M., 2018. Technical Note: Asteroid Detection Demonstration from SkySat-3* B612 Data using Synthetic Tracking, 17.

Zhang, K., Sun, J., Snavely, N., 2019. Leveraging vision reconstruction pipelines for satellite imagery. In: ICCV Workshop on 3D Reconstruction in the Wild (3DRW).